ABSTRACT

Title of Document: TOWARDS THE USE OF DIELECTRIC
ELASTOMER ACTUATORS AS
LOCOMOTIVE DEVICES FOR
MILLIMETER-SCALE ROBOTS

Justin Pearse, Master of Science, 2012

Directed By: Professor Dr. Elisabeth Smela,
Department of Mechanical Engineering

Dielectric elastomer actuators (DEAs) are electromechanical transducers that are promising for small scale applications. The work presented in this thesis seeks to develop DEAs as an actuation technology that would serve the purpose of ambulating millimeter-scale robots in a robust and predictable manner. To begin, the "planar" DEA configuration was characterized and the performances of various elastomers were investigated. Then, based on the requirements of a proposed robot walking gait, two principles were examined as means of converting in-plane actuation strain to bending actuation. Bending DEAs were fabricated and tested, and a maximum end displacement of 1.5 mm was achieved for a 10 mm long sample. Bending actuator design was optimized by maximizing both speed and payload capabilities. Finally, some challenges facing the design of robots ambulated by DEAs were outlined; of particular note is the DEAs' electrostatic interaction with each other and their surroundings.

TOWARDS THE USE OF DIELECTRIC ELASTOMER ACTUATORS AS
LOCOMOTIVE DEVICES FOR MILLIMETER-SCALE ROBOTS

By

Justin Daminabo Pearse

Thesis submitted to the Faculty of the Graduate School of the
University of Maryland, College Park, in partial fulfillment
of the requirements for the degree of
Master of Science
2012

Advisory Committee:

Professor Elisabeth Smela, Advisor/ Chair
Professor Sarah Bergbreiter
Professor Satyandra K. Gupta

Dedication

This work is dedicated to:

My parents Justus Donye and Ngozi Soba, for their endless sacrifice without which

all of this would not be possible, and

My siblings Alfred Dagogo and Jennifer Soba, for being… well, my siblings.

Acknowledgements

Table of Contents

List of Tables

List of Figures

Chapter 1: Introduction

1.1 Research Motivation

Millimeter-scale robots allow for the exploration of small, enclosed spaces that are typically unreachable. For example, they could engage in humanitarian efforts such as search and rescue operations in the aftermath of natural disasters. Swarms of millimeter-sized robots capable of cross-communication and autonomous formation could be sent to search for survivors. These infiltration capabilities may also be used to assist in counterintelligence and national security efforts. Furthermore, these robots could serve as platforms for biological research into social insect swarming, task-accomplishment, and behavior patterns. For these robots to operate successfully, they must possess robust, predictable, and resilient means of ambulation.

1.2 Literature Review of Actuation Technologies

A number of attempts have been made to develop suitable actuation technologies that operate within the inherent size scale limitations of milli-to-micro-scale robotics. Magnetic actuators offer high controllability and flexible robot design [1] using programmed magnetic anisotropy to actuate robot body segments in separate directions with a common, externally-applied magnetic field (Figure 1.1a). However, because one must assemble the set-up needed to generate the requisite magnetic field *a priori* at the robot's operation location, the applications for this technology are limited.

Piezoelectric actuators have shown great promise because of their compact size, high strain and force output, and high bandwidths [2, 3]. As such, groups such as Harvard Microrobotics Lab and the Army Research Lab (ARL) have utilized these actuators in winged microrobotic insects (Figure 1.1b and c). These actuators, however, are brittle and exhibit low displacements when not amplified by a mechanical transmission or operating at resonance.

Thermal actuators are commonly used because of their high force output (increased payload capabilities) [4] and relative ease of fabrication. Perhaps the best known work is the thermally-actuated robot designed by Ebefors et. al [5] (Figure 1.1d) that demonstrated walking speeds of up to 6 mm/s with a total payload of 2500 mg. Erdem et. al [4] developed a thermally-actuated microrobot (Figure 1.1d) capable of 2-DOF movement with speeds up to 0.18 mm/s and a payload of up to 3.5 g. However, thermal actuators require high currents for Joule heating and suffer from low efficiencies, thus requiring tethers and limiting the use of on-board power. Also, the thermal lag (i.e. time-limited heat dissipation hindering high-frequency operation) serves to negatively impact ambulation speed.
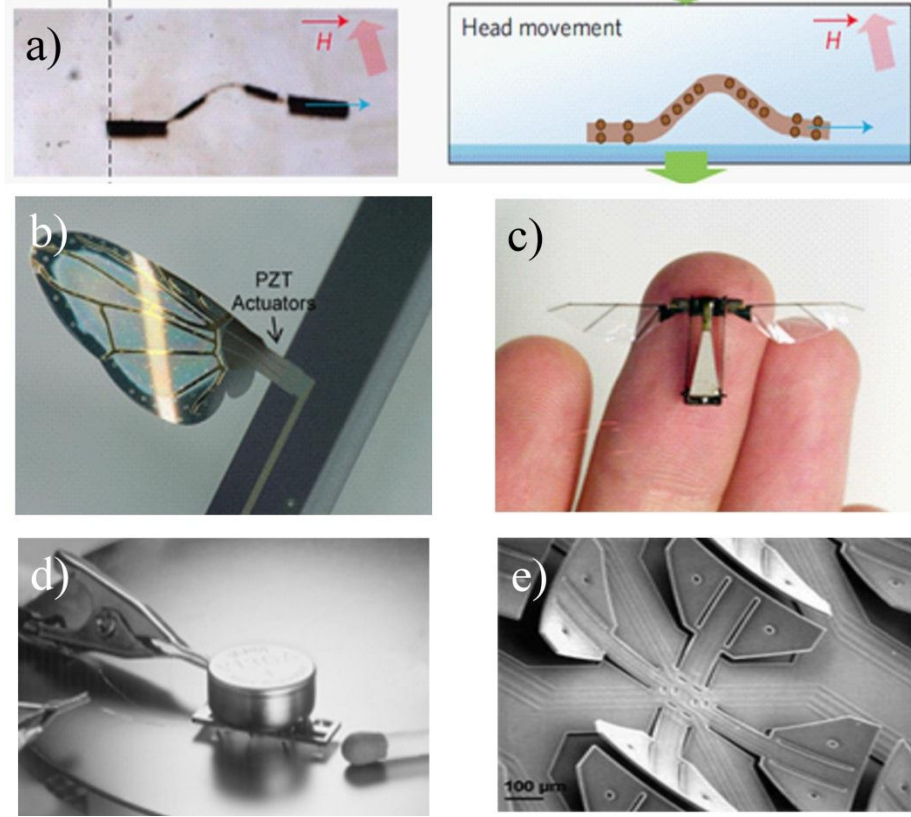
Figure 1.1: Examples of micro-scale robots. (a) Magnetically-operated inch-worm robot [1]. (b) Micro-machined piezoelectric wings operated at resonance [2]. (c) Harvard microrobotic fly showing piezoelectric actuator and mechanical transmission [3]. (d) Thermally-actuated walking robot developed by Ebefors et. al, shown tethered and supporting payload [5]. (e) SEM image of singular "motion pixel" by Erdem et. al, showing bi-directional thermal cilia actuators. The microrobot features two arrays of these pixels [4].

A class of actuators called dielectric elastomer actuators (DEAs) have shown the potential to achieve the displacements and efficiencies required for autonomous ambulation [6]. These soft, polymer-based actuators operate using high voltage and low current, and feature relatively large strains (>5%) [7].

1.3 Dielectric Elastomer Actuators (DEAs)

DEAs are structures composed of an elastomer (dielectric) sandwiched between two electrodes. A typical DEA at rest is illustrated in Figure 2.1a. When high voltage (kV) supplied to the electrodes, an electric field is generated across the elastomer as

3

opposite charges build in the electrodes and become attracted to one another. These electrodes compress the elastomer layer in the out-of-plane direction, and if the electrodes are compliant (i.e. stretchable) they allow the elastomer to expand in-plane, conserving volume. This in-plane expansion or actuation is shown in Figure 2.1b.

(a)

(b)
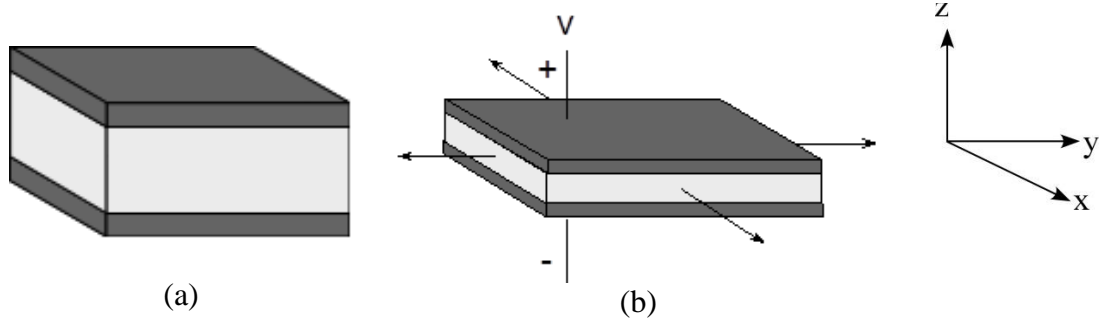
Figure 1.2: Operating principle of DEAs. (a) Actuator at rest before voltage application. (b) DEA planar actuation in response to applied voltage V.

Since DEAs are typically modeled as simple electrical capacitors with zero current leakage, the stored electrical energy upon voltage application U and the force P imparted by the resulting electric field are given respectively as:

$$U = \frac{1}{2}CV^2 = \frac{1}{2}\varepsilon_0\varepsilon_r V^2 \frac{A}{h} \qquad (1.1)$$

$$P = -\frac{\partial U}{\partial h} \qquad (1.2)$$

where C is the capacitance, V is the applied voltage, ε_0 is the vacuum permittivity (8.85×10^{-12} F/m), ε_r is the relative dielectric permittivity of the elastomer material,

A is the cross-sectional area perpendicular to the electric field, and h is the elastomer film thickness. If constant volume is assumed ($A \times h = constant$), the out-of-plane (z-direction) actuation stress σ_z in a DEA for small strains ($< 20\%$) is given by [8]:

$$\sigma_z = \frac{P}{A} = -\varepsilon_0 \varepsilon_r \left(\frac{V}{h}\right)^2 \tag{1.3}$$

so that the in-plane stresses S_x and S_y are related to the out-of-plane strain S_z by:

$$S_x = S_y = -v S_z = v \left(\frac{\varepsilon_0 \varepsilon_r}{E}\right) \left(\frac{V}{h}\right)^2 \tag{1.4}$$

where v is the Poisson's ratio of the elastomer and E is the elastomer's elastic modulus.

1.4 DEA-Ambulated Robots

At the macro-scale, DEAs have been employed as actuators for walking robots. For these applications, DEA films are commonly rolled to form linear actuators ("roll" configuration). In the case of Flex 2 [9] (Figure 1.3a), the roll DEAs move the legs analogous to the function of muscles attached to bone. In the cases of Skitter [9] (Figure 1.3b) and MERbot [6] (Figure 1.3c), the roll DEAs act as the legs themselves. At the millimeter-scale, DEAs have also been utilized (in the "membrane" configuration) for hopping robots [6] (Figure 1.3d).
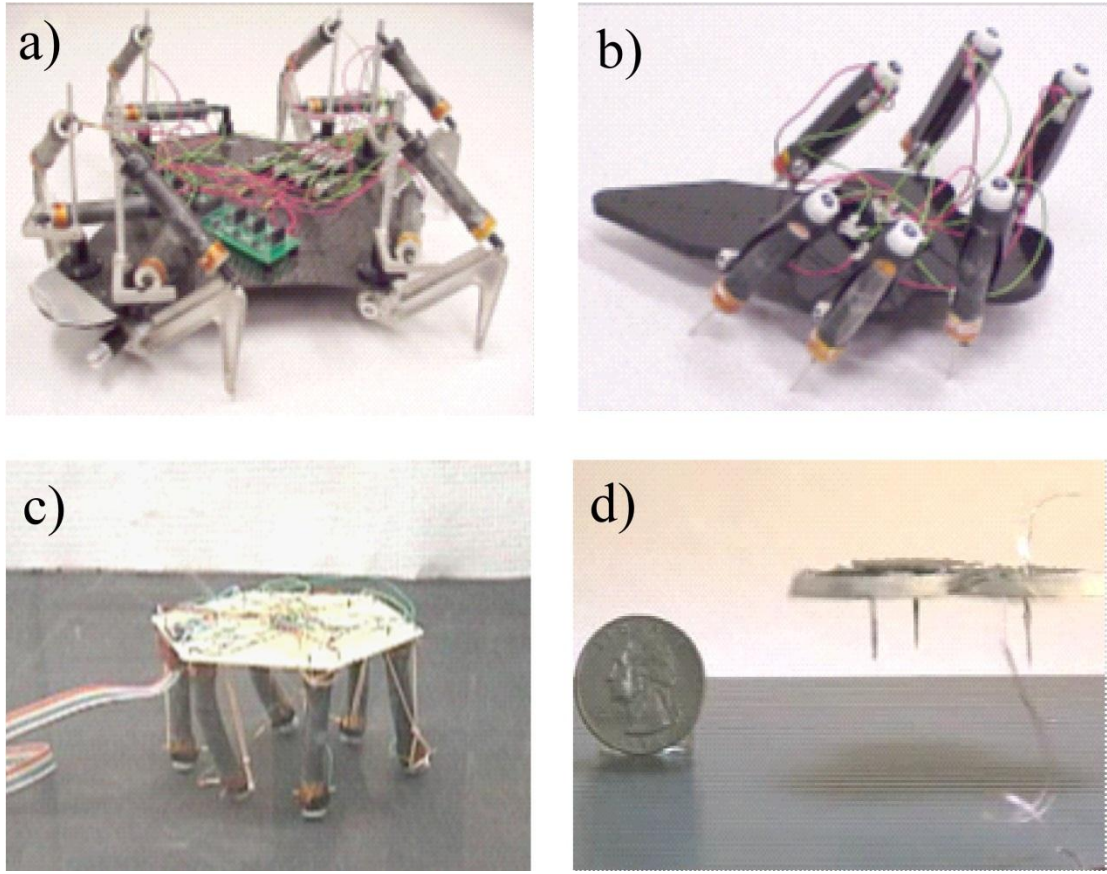
Figure 1.3: Examples of DEA-ambulated robots. (a) Flex 2, a 6-legged biomimetic robot weighing 470 g with a body length of 36 cm, uses roll DEA as muscles [9]. (b) Skitter, a 6-legged robot using roll DEAs as legs themselves [9]. (c) MERbot, a hexapedal robots using 2-DOF roll DEAs as legs [6]. (d) Simple hopping robot actuated by DEA diaphragms (membranes) [6].

However, macro-scale robots such as those presented in Figure 1.3a-c are complex, and are too large to fit in the small spaces encountered in some of the potential applications. There is an interest in exploring the use of DEAs at increasingly smaller scales with simpler structures. Therefore, this research moves away from DEA configurations such as rolls and membranes, which require frames, and towards simpler configurations such as uniaxial free-film (planar) [10] and bending actuators [11, 12].

The purpose of the research presented in this thesis is to lay the foundation for the implementation of meso-scale DEAs as locomotive devices for millimeter-scale robots. In Chapter 2, the planar DEA configuration is characterized (the simplest form of DEAs that do work on external objects), and the performance of polydimethysiloxane (PDMS) as a DEA elastomer material is examined. For comparison, DEAs comprised of two other commonly used elastomer materials (TC-5005 and VHB-4905) are also tested. In Chapter 3, the need to convert in-plane strain to bending displacement is discussed via the proposition of a walking gait for a DEA-ambulated robot. Two different principles are explored as means of achieving these results. In Chapter 4, through the use of MATLAB's *fminimax* solver, the performance of DEA legs is optimized. This is achieved by maximizing walking speed and payload per leg, two conflicting objectives. The bending DEAs used in the analysis are based on designs presented in Chapter 3, whose bending is modeled using Timoshenko bilayer theory and whose load-bearing capacities are modeled using slender column mechanics theory. In Chapter 5, some challenges involved with attaching the bending DEAs to a robot body are detailed. Specifically, DEA interactions with their surroundings, and the use of real-estate on the robot body for mechanical and electrical connections pose problems that hinder the realization of DEA-ambulated millimeter-scale robots. Chapter 6 summarizes and concludes the research presented in this thesis, and suggests future work.

Chapter 2: Characterization of Planar PDMS Dielectric Elastomer Actuators

2.1 Authorship & Contributions

The work presented in this chapter of the thesis was adapted from an eponymous paper in preparation (at the time of this writing), co-written by me, along with my former colleague, Dr. Mark Kujawski, and my research advisor, Dr. Elisabeth Smela. I performed experiments and analyzed data for the relative dielectric permittivity, actuation strain, and PDMS load curve sections. Dr. Kujawski performed experiments, analyzed data for the creep section, and collected data for the modulus section. Dr. Smela contributed some general data analysis, text writing, and editing work.

2.2 Introduction

For DEAs to be used as actuators for robotics applications, their behavior must be well characterized. Ideally, the dielectric elastomer used in the fabrication of these actuators should possess minimal creep, produce significant actuation strains, and operate at high actuation frequency with low attenuation.

In this chapter, we examine the uniaxial free-film (planar) configuration of DEAs, so-called because actuation is only observed in-plane and the film is not pre-stressed or pre-strained before voltage application. In addition, the silicon-based elastomer polydimethylsiloxane (PDMS) is examined for its use in small-scale robotics applications. PDMS is promising because it can be formed into films of desired thickness and shape, unlike elastomers commercially available in tape form. Other

elastomers such as VHB-4910 [13], TC-5005 [14], and HS III RTV [10], as well as free-film DEAs based on these materials have been previously characterized. The properties of PDMS and the actuation of PDMS-based DEAs are compared to the two most frequently used dielectric elastomers, VHB-4905 and TC-5005. The relative dielectric permittivities, elastic moduli, and creep of the elastomers were measured.

Also measured was the actuation strain as a function of electric field strength; we show that the electrostatic (Maxwell) stress model (Equation 1.4) is too simple to fully describe the behavior of the planar configuration. We conclude the chapter by investigating the characteristic load curve of a planar PDMS DEA.

2.3   Experimental

2.3.1   Elastomer Sample Preparation

PDMS (Sylgard 184, Dow Corning) and TC-5005 (BJB Enterprises) are silicones, and VHB-4905 (3M) is an acrylic. The VHB-4905 is commercially available in the form of a tape 12.5 mm wide and 500 μm thick. PDMS and TC-5005 are prepared by combining a pre-polymer and a curing agent.

Sylgard 184 pre-polymer and its curing agent were mixed at a 10:1 ratio by weight and vacuum-desiccated for 30 minutes to remove air bubbles. Films were formed by spin-coating this solution onto glass slides at 750 rpm for 60 seconds, followed by vacuum-desiccation for 5 minutes and baking on a hotplate at 95 °C for another 5

minutes. The resultant PDMS films were 100 ± 21 μm thick, determined by surface profilometry (Dektak^3 ST).

TC-5005 samples were also prepared by mixing a 10:1 ratio by weight of resin and curing agent. TC-5005 was not spin-coated because curing of thin films is inhibited by oxygen. Instead, after vacuum-desiccation for 30 minutes, TC-5005 was cast into thick films, 830 ± 40 μm as measured with a handheld micrometer (L.S. Starrett Co., No. 120AM), in polyethylene petri dishes and cured at room temperature for 48 hrs.

The elastomers were cut into strips of 45 x 12.5 mm. One end of each strip was glued onto a glass microscope slide using a photo-curable adhesive (Loctite 3108), and the other end was glued onto a 12.5 mm x 12.5 mm piece of transparency sheet (3M), leaving a 20 mm long, 12.5 mm wide section in the center that was free to stretch (Figure 2.1).
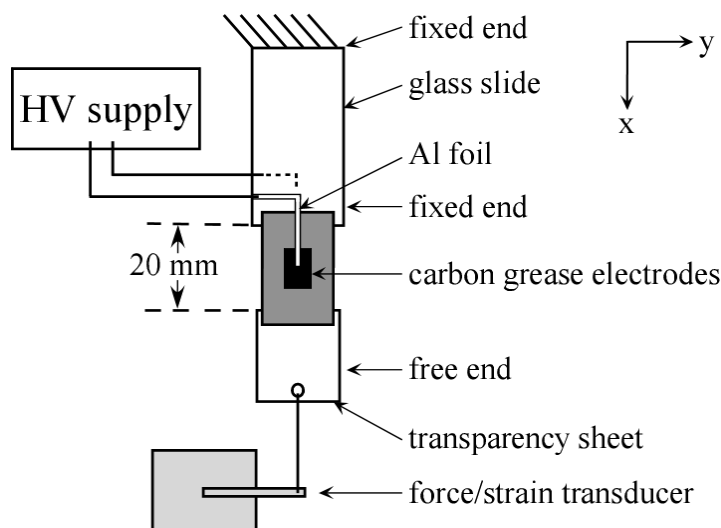
Figure 2.1: Planar DEA configuration and experimental setup.

2.3.2   DEA Fabrication and Electrical Connections

Carbon grease (MG Chemicals) was utilized as the electrode material because it could be used with all three elastomers. The active area of the DEA (i.e., the area of the elastomer sandwiched between both electrodes) was maintained at approximately 0.8 cm^2. Stencils 9.3 ± 0.2 mm long and 8.3 ± 0.1 mm wide were used to pattern the carbon grease electrodes, leaving approximately 2 mm of "passive" material between the electrode and the edge of the film to prevent electrical arcing from one electrode to the other. When the carbon grease was applied closer to the edges, arcing occurred around the edge of the elastomer (not through it) at relatively low voltages. It is worth noting that this failure is different from dielectric breakdown, for which the failure occurs within the electrode area. Carbon grease was applied over the stencil to a thickness of approximately 1 mm using a spatula, and then the stencil was removed. The top and bottom stencils were aligned by eye.

The experimental setup is shown in Figure 2.1. Electrical connections to the grease were made using thin (approx. 2 mm wide) strips of Al foil bent into an arc that adhered to the grease electrode at one end and were connected to a high voltage power supply (HV Rack, UltraVolt) via wires attached by clips at the other.

2.3.3   Measurement of Actuation Strain

A force/strain transducer (Aurora Scientific Inc., model 300C, ASI Dual-Mode Lever System) applied and measured forces and displacements, which were later converted to stress and strain using the elastomer dimensions. The resolutions of the transducer

11

were 1 μm and 3 mN for distance and force, respectively. Elastomer films and DEAs were suspended vertically by clamping the glass slides above the transducer arm (Figure 2.1). The transparency sheets were connected to the transducer using suture thread looped through small holes in the transparency and in the transducer arm. A 1 g force (corresponding to approximately 8.2kPa for PDMS, 1 kPa for TC-5005, and 1.6 kPa for VHB-4905 at the film thicknesses utilized in this work) was applied by the transducer to hold the samples taut at the start of the measurement.

2.3.4 Measurement of Relative Dielectric Permittivity

Dielectric permittivities were measured with a dielectric analyzer (TA Instruments DEA 2970). Elastomer samples of 12.5 mm × 12.5 mm were placed onto the bottom ceramic plate, at the center. On both the top and bottom plates were 5 mm diameter gold (Au) electrodes. The top plate was lowered to bring both electrodes into mechanical contact with the elastomer. A compressive load of 1 N was applied to the sample, and ε_r was measured at 25 °C using a 10 mV signal at three frequencies (f = 1, 10, 100 Hz).

2.3.5 Actuator Load Curve Measurement

Actuation strain was measured versus applied mechanical load for PDMS DEAs. Under large axial loads, there was some inward deformation of the elastomer film in the y-direction (necking, shown in Appendix B.1). This deformation resulted in a smaller gap between the electrode and the edge of the sample, increasing the probability of device failure via arcing. To compensate for this, and also to keep the applied voltages within the 10 kV limit of the high-voltage source, and displacements

and forces within the 10 mm displacement and 100 mN force ranges of the force-strain transducer, the dimensions of these samples were modified. The non-electroded area at the edges of the film was increased from 2 mm to 3 mm (decreasing the active area to 6.3 mm wide by 6.3 mm long), and the film thickness was decreased from 100 μm to 35 ± 3 μm so that the voltages could be lowered while maintaining the same E field.

The actuators were mounted as shown in Figure 2.1 and subjected to uniaxial stresses ranging from 0.02 MPa to 4.3 MPa (loads of 1-40 g). At each load, the length of the elastomer L_0 (between the glass slide and the transparency) was recorded before the voltage was applied. The force-strain transducer measured the change in displacement ΔL upon turning the voltage on and off, and the actuation strain was calculated as $\Delta L / L_0$.

The force-strain transducer applied loads from 0.02 MPa to 1 MPa. Higher loads were achieved by supplementing the force-strain transducer, set to 0.7 MPa, with weights hung onto the bottom of the transparency sheet using a hook. The applied voltage was adjusted based on the elastomer thickness at each load to produce an electric field of 40 V/μm. The elastomer thickness was determined with mechanical calipers having a resolution of 2 μm (L.S. Starrett Co., No. 120AM).

2.4   Results & Discussion

To predict the actuation strain from Equation 1.4 for a given electric field, one needs to know ε_r and Y. Therefore, characterization began with the measurement of these

material constants for PDMS, VHB, and TC-5005. Since actuators are generally required to do work, creep under load was also measured. The remainder of the section characterizes the planar DEA configuration including actuation strain as a function of electric field, and actuation strain as a function of load (load curves).

2.4.1 Relative Dielectric Permittivity

Although often assumed to be constant, the permittivities of elastomers have been shown to depend on actuation frequency [15, 16], electrode material [16, 17], temperature [17], pre-stress or load [17, 18], and applied electric field [19]. In this work, the dielectric permittivities of the three elastomers were measured as a function of the frequency of the applied voltage at constant temperature (25 °C) and using the same electrode material. A compressive load of 1 N was applied to the samples to hold them in place during testing. Three samples of each material were tested. The results are shown in Figure 2.2.
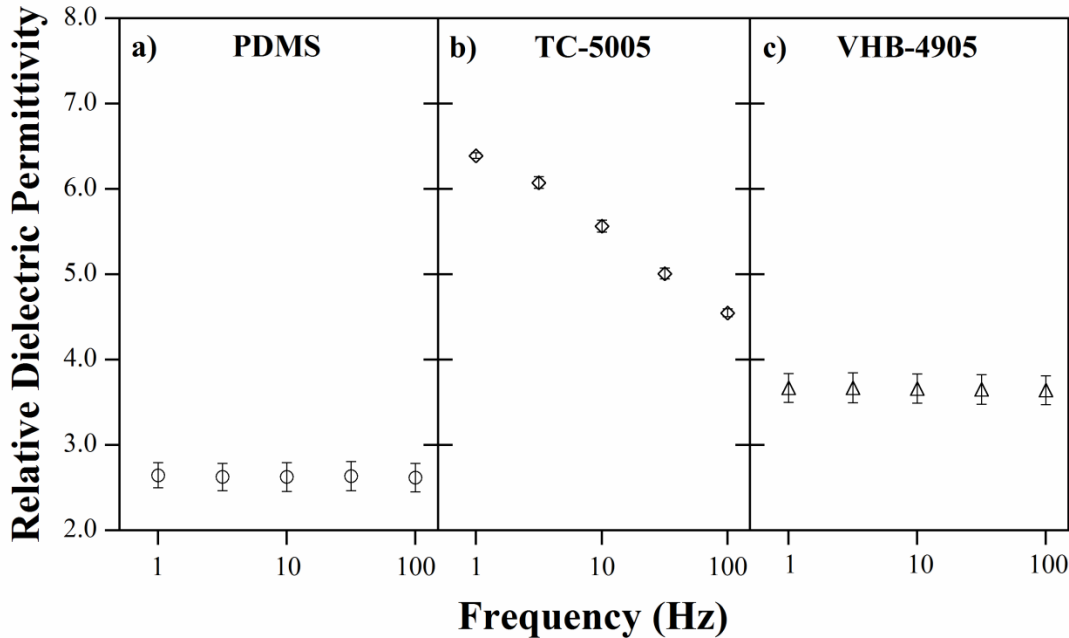
Figure 2.2: Relative dielectric permittivity (ε_r) as a function of frequency.

As is evident from Figure 2.2a, PDMS had the smallest ε_r of the three elastomers, varying from an average of 2.65 at 1 Hz to 2.62 at 100 Hz. Considering the error between samples, we can conclude that ε_r for PDMS is frequency independent in this range. The values noted here closely match those previously reported in the literature: 2.65 (f = 100 Hz, 100 kHz) specified by the manufacturer (Dow Corning).

TC-5005 had the highest permittivity, which is desirable for DEAs according to Equation 1.4. At 1 Hz, the average ε_r was 6.39, or 2.4x greater than that of PDMS under the same conditions. However, as shown in Figure 2.2b, it was strongly frequency-dependent, dropping from 6.39 at 1 Hz to 4.55 at 100 Hz. This means that the actuation strain would deteriorate significantly as the DEA was operated at faster rates. For comparison, Carpi et al. [14] reported a value of 4.6 at 10 Hz.

The ε_r of VHB-4905, like that of PDMS, was frequency independent as shown in Figure 2.2c. This dependence (or lack thereof) has been noted in the literature, although its extent varies: Ma et al. [20] concluded that there was no significant change in ε_r with frequency (100 Hz – 100 kHz) while Kim et al. [15] showed no variation between 0.1 Hz and 10 Hz, and a 10 % decrease between 10 Hz and 10 kHz. Kofod et al. show similar results to Kim et al., with no ε_r dependence between 0.1 Hz and 10 Hz, and a slightly decreased (0.2 %) value at 100 Hz. The manufacturer specified a ε_r of 3.21 at 1 kHz (3M), Wissler et al. [21] reported 3.34 at 100 Hz, and McKay et al. [19] gave values from 3.1 to 6.6. It has been suggested that changes in the proprietary material composition might be to blame for the wide variations [21].

The frequency dependence of the TC-5005 and independence of PDMS and VHB-4905 are likely due to variations in dipolar relaxation times [17, 22]. Because it takes some time for the dipole segments in the polymer to align with the applied electric field, and recover to their original position upon field removal, at low frequency, one would expect little variation in dielectric permittivity, rendering it a constant. At higher frequencies, the dipoles do not have enough time to return to their original positions and ε_r appears frequency-dependent. It has been noted in literature that these relaxation times are material dependent [15].

2.4.2 Elastic Modulus

The elastic moduli of the three elastomers have previously been reported (Table 2.1), but for PDMS and TC-5005 they vary based on sample preparation (the stiffness of PDMS increases with curing agent concentration, and the stiffness of TC-5005 decreases with plasticizer concentration) and even for VHB-4905 there is a considerable spread in the values. Moreover, an elastic modulus is only defined for the initial linear region of a stress-strain curve. Elastomers may not have such a linear region, and in DEAs the elastomer can undergo strains well outside this region, where the slope of the stress-strain curve may be nonlinear. The slope of the stress-strain curve is more generally known as the *tangent modulus*, and is specified at a particular strain. For the purposes of this work, we will continue to use the symbol E to represent the modulus, tangent or elastic.

Table 2.1: Tangent moduli at 5% strain of the three elastomers.

Elastomer	Measured tangent modulus (MPa)	Previously reported modulus values (MPa)	(Percent strain during measurement) References
PDMS	1.06 ± 0.02	0.75 - 2.6	[23], (40%) [24]
TC-5005	0.103 ± 0.004	0.062 - 0.10	(210%) [25], (100%) [14]
VHB-4905	0.165 ± 0.002	0.18 - 0.80	[26], (30%) [20]

The tangent moduli for the three elastomers were determined at moderate strain (5%) under identical conditions to facilitate later comparisons in this paper. The force/strain transducer applied increasing displacements at a rate of 0.1 mm/second to the elastomers while the force was measured. Values were converted to strain and stress using sample dimensions. The tangent moduli were calculated from the slope of the stress-strain curve at 5% strain by fitting a straight line to the points between 4%

17

and 6% strain. The curves for each elastomer are shown in Figure 2.3, and the tangent moduli are given in Table 2.1. Based on the force-strain transducer's force resolution, the uncertainty in stress measurements for PDMS, TC-5005 and VHB-4905 were ± 2.4 kPa, ± 0.3 kPa and ± 0.5 kPa, respectively. The initial stress at zero strain is due to the small tension applied to the films to keep them taut.
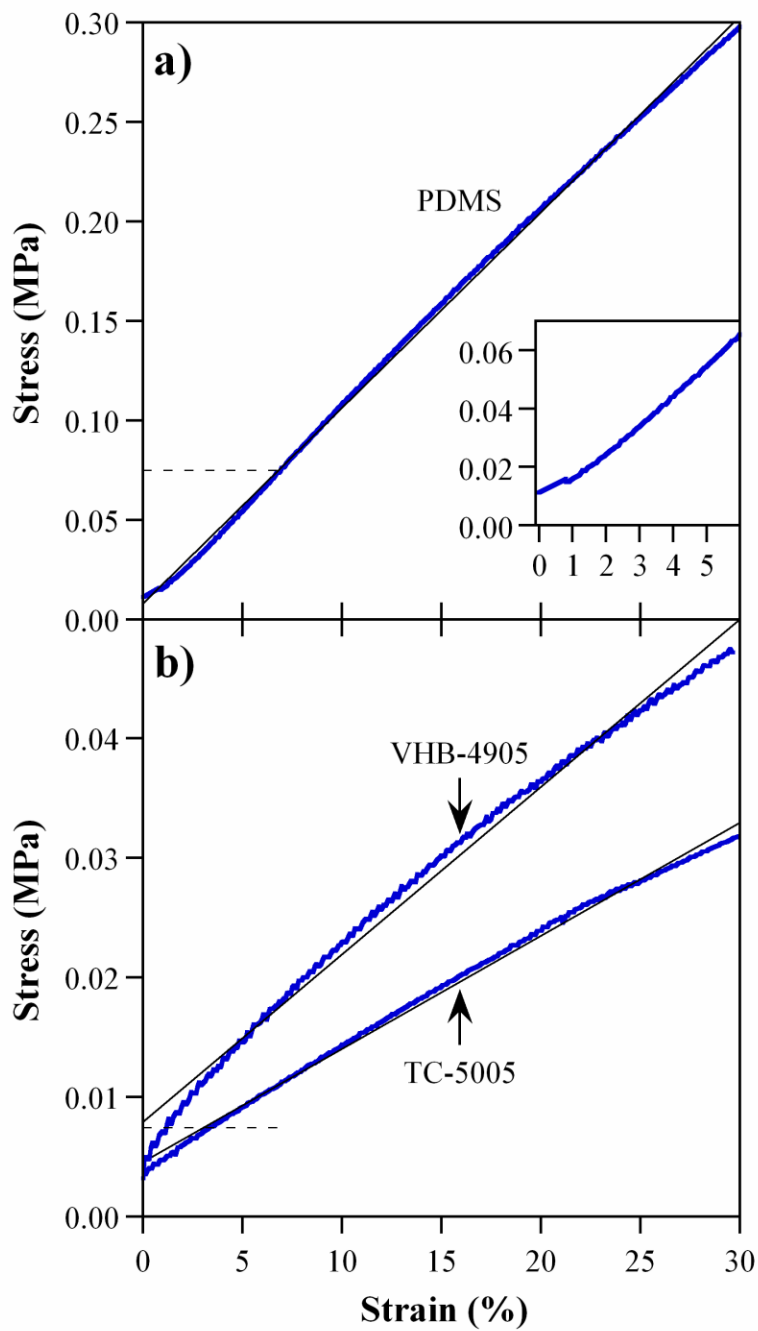
Figure 2.3: Stress as a function of strain (thick blue lines) for the three elastomers. Linear fits (thin black lines) and 75 kPa pre-stresses (applied in experiments later in this chapter) (horizontal dashed lines) are also shown.

Figure 2.3 shows that the stress-strain curves are nonlinear throughout this entire

range of strain, although PDMS had the most linear behavior. It is therefore necessary

to use the tangent modulus, instead of elastic modulus, and to specify the strain at which the value is obtained. The behavior may become linear outside of this range, under high pre-strain, but the assumption of a constant modulus and linear behavior may be invalid and needs to be justified for the particular experimental conditions.

PDMS is an order of magnitude stiffer than TC-5005 and VHB-4905. The moduli are compared with previously reported values in Table 2.1, and the values are similar. More direct comparisons with the literature are difficult because the stress-strain curves are often not provided, and the strains at which the moduli are obtained are not usually specified. The PDMS and VHB-4905 values are on the low side of the reported range, while TC-5005 is somewhat higher. It is not clear why the reported range for VHB, obtained in tape form, is so large. As previously noted, material formulation, strain, and non-linearity are possible contributors.

As shown in the inset of Figure 2.3a, the stress-strain curve of PDMS consistently showed a knee at 1% strain, the tangent modulus increasing from 0.48 MPa below the knee to 1.06 MPa above it. Depending on the strain range used for a particular application, this strain hardening may need to be taken into account. VHB-4905 and TC-5005 (Figure 2.3b) do not exhibit this behavior; in fact, VHB-4905's tangent modulus drops from 0.32 MPa at 1% strain to 0.13 kPa at 30% strain.

All other things being equal, the 6-10x higher modulus of PDMS will result in lower actuation strains than can be achieved with TC-5005 or VHB-4905. It should be

noted that the modulus can be lowered for both PDMS and TC-5005 by adding less of the curing agent: a 20:1 ratio of PDMS resin to curing agent exhibits a tangent modulus of 0.79 ± 0.04 MPa at 10% strain.

2.4.3 Creep

Creep is the tendency of a solid material to continue to deform in response to a constant applied force [27]. Creep behavior for VHB-4905 has been previously reported in literature; Jhong et al. [28] assumed a non-linear (logarithmic) dependence of material strain on creep and developed empirical parameters to account for its effects, and Jordan et al. [29] measured the creep in the actuation strain of a VHB-4905 DEA. Creep can pose problems for DEAs: depending on the device configuration and application, creep could necessitate continuous counteracting adjustment of the voltage in order to maintain a given strain, and it introduces memory effects that complicate actuation repeatability and control [28]. Creep was determined by applying a stress of 75 kPa to the elastomer films in an isotonic (constant force) experiment and measuring the strain over 10 hours with the force/strain transducer. The results are shown in Figure 2.4. Based on the force-strain transducer's displacement resolution, the uncertainty in creep strain measurements was $\pm 0.0025\%$.
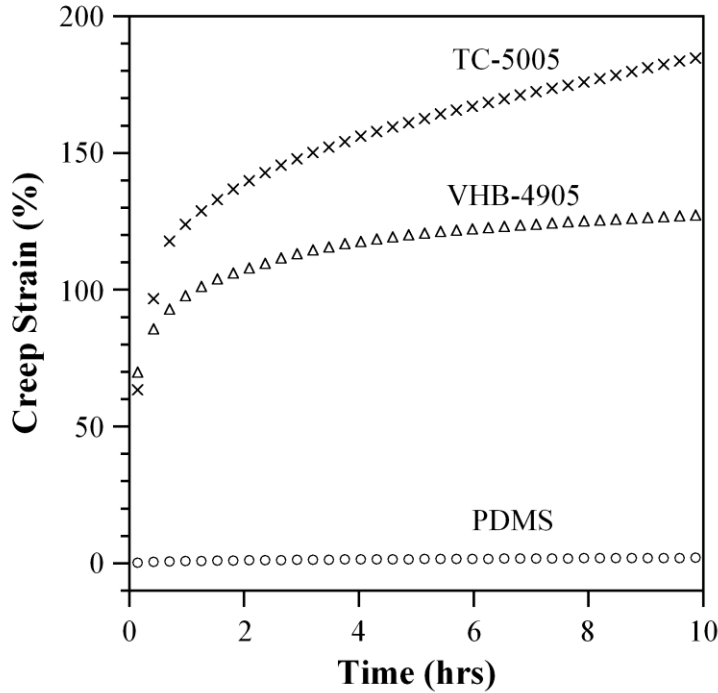
Figure 2.4: Creep strain as a function of time for the three elastomers under a uniaxial load of 75 kPa.

The total creep after 10 hrs was 2% for PDMS, 185% for TC-5005, and 130% VHB-4905. Before the 6 hour mark, the creep rates were non-linear, but after 6 hours the creep rates become more or less constant: 0.08% /hr for PDMS, 4.5% /hr for TC-5005, and 1.3% /hr for VHB-4905, respectively. The general shape of the curve in Figure 2.4 is similar to that published by Jordan et al. [29], but because creep is load-dependent [30], a more direct comparison was not possible.

While TC-5005 had a higher ε_r (2.5x) and lower modulus (10x) than PDMS, leading one to expect a much larger actuation strain (25x), it exhibited the largest creep (two orders of magnitude greater than PDMS). The data suggest that TC-5005 can therefore only be used in low-load applications or in situations where creep does not significantly interfere with the desired performance (and where its frequency-

dependent ε_r is also not a factor). The issues are similar for VHB-4905. PDMS-based

DEAs suffer from lower strain, but should have greater controllability and be able to

exert greater actuation force.

2.4.4 Actuation Strain as a Function of Electric Field

We turn now to characterization of the planar DEA configuration, beginning with the

actuation strain performance under an electric field. The Maxwell model of Equation

1.4 predicts that strain is proportional to $(V/h)^2$ and this has been confirmed in

numerous prior studies with many different elastomers and device configurations.

Equation 1.4 assumes freely moving (unclamped) boundary conditions, as if the film

were suspended in mid-air. However, in our testing the DEA was rigidly clamped on

two sides (Figure 2.1) and held straight by the force-strain transducer. In addition, the

active (electroded) area of the DEA did not extend all the way to the edge of the

elastomer. The measured strain is therefore reduced by the electrode-free "passive"

areas at the vertical edges, which act as springs in parallel [10]. These regions may

also result in an out-of-plane component to the movement of the active area, which

could bulge outward like a membrane-type device at this low loading. Thus, the

measured actuation strains were expected to be lower than predicted by the model.

DEAs made from the three elastomers were actuated with increasing fields, applied in

two consecutive 10-40 sec on/off cycles, the time depending on how long it took for

the displacement to stabilize. The failure thresholds for the DEAs were 55 V/μm for

PDMS, 10 V/μm for TC-5005 and 15 V/μm for VHB-4905. Because the minimal

load on the samples did not cause significant creep and because strains were small,

the sample thickness measured after mounting but before actuation was used to

calculate the electric field applied, without correction. Samples were allowed to relax

for 1 hour after mounting, before the electric field was applied. The actuation strain

was obtained for three samples of each elastomer type. The change in length during

the second voltage on/off cycle was used because the actuator did not always return to

its starting position after the first cycle, but initial positions were stable thereafter.

Actuation strain is shown as a function of $(V/h)^2$ in Figure 2.5.
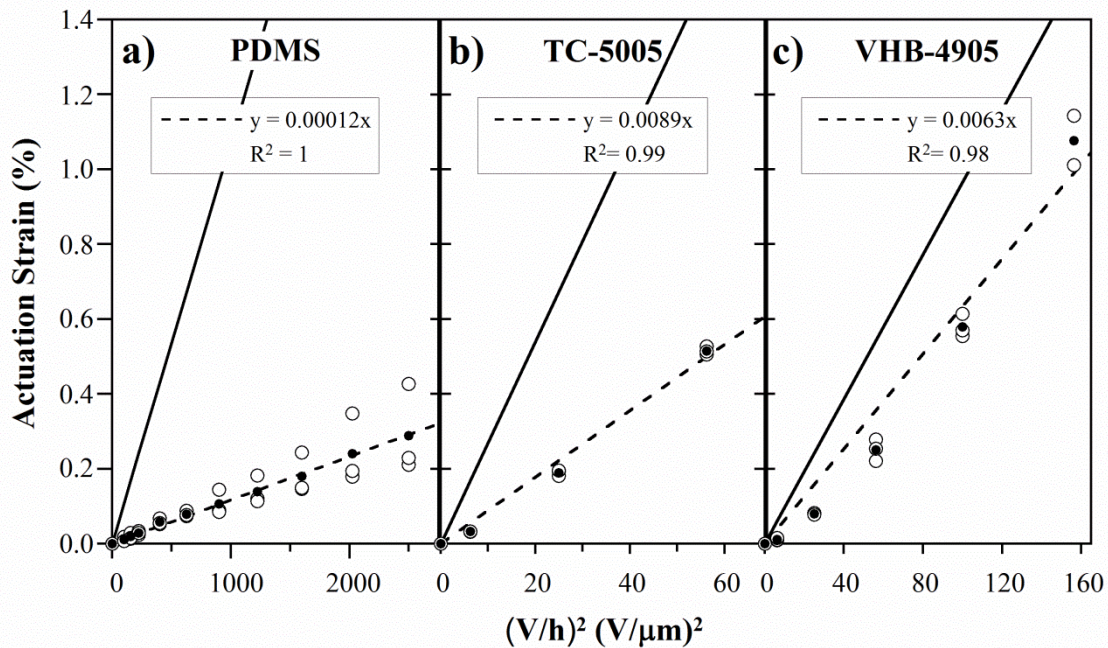
Figure 2.5: Actuation strain as a function of the square of the electric field for three DEAs made from each elastomer (open circles). Note that the x-axes differ. The dotted lines are linear fits to the average strain (filled circles), and the solid lines are the in-plane strains expected from Equation 1.4. The samples were held taut by a 1 g load (corresponding to stresses of 8.2 kPa for PDMS, 1 kPa for TC-5005, and 1.6 kPa for VHB-4905).

As expected from its low modulus and large ε_r, TC-5005 had the largest slope. It was

followed by VHB with approximately 2/3 of that value, which is twice as high as

predicted from the measured values, relative to TC-5005. The slope for PDMS was

approximately 75x smaller, although only 25x smaller was predicted. Linear fits to

the data give reasonable R^2 values, although there is a small upward curvature, particularly noticeable in Figure 2.5c for VHB-4905. As is evident from the figure, the Maxwell model over-predicted the actuation strain for planar DEAs of all three materials. This is because the model is too simple and does not consider boundary conditions and other geometric effects.

It has been pointed out in prior work that actuation strain in a particular device should not be expected to follow Equation 1.4 because the model does not take into account the complexity of the stress state induced by the boundary conditions and/or device configuration [8, 31]. The former was noted by Ma et al. [20] and also Yang et al. [10]. The effects of device configuration have been seen in roll actuators, which may behave as if the radius were fixed, transferring the decrease in thickness upon actuation to a greater-than-expected strain in the axial direction [31]. Electrode material and thickness have been shown to affect actuation performance as well [32].

If ε_r and Y are strain-dependent or temperature-dependent, these relationships should also be taken into account [21, 32-34], as should any hyperelastic behavior [7]. In one case, this was done by introducing an electrostrictive term to account for the changing dielectric constant [35], and in other cases curve-fit factors or additional terms have been added to the equation [32, 34].

As shown in Figure 2.5, the upper limits of strain were not determined by dielectric breakdown but rather by device failure due to shorting around the samples' edge,

from one electrode to the other. The largest strain was 1.1%, attained for VHB-4905 at an electric field of 12.5 V/μm. In comparison, TC-5005 reached a maximum strain of 0.5 % at 7.5 V/μm, and PDMS a strain of only 0.22% at 50 V/μm. These are not necessarily the maxima that can be reached by uniaxial actuators of these materials: as previously mentioned, the boundary conditions likely play a role that is not yet fully understood.

2.4.5   Future Elastomer Materials Testing

From the results of measuring the relative dielectric permittivity, tangent modulus, creep strain, and actuation strain of the frequently used DEA elastomers (Sections 2.4.1 - 2.4.4), it is evident that none of the three materials are truly the best for DEA fabrication and performance. Instead, the qualities of an ideal DEA elastomer material are shared amongst the three: PDMS possesses low creep, good frequency response (ε_r frequency-independence) and design flexibility, while TC-5005 and VHB-4905 have low tangent moduli, and offer large actuation strains at low electric fields. Since such an ideal elastomer material is yet to be identified, the experimental setup and testing procedure detailed in these sections could serve as a new protocol for future elastomer materials testing. This protocol is novel because it emphasizes the in-situ measurements of material properties pertinent to the performance of planar DEAs. In order words, all material properties (except ε_r due to equipment limitations) were measured using samples under the same conditions and in the configuration as the final planar DEAs. By performing these tests on any prospective material, one can draw comparisons with the frequently used elastomers, and gain insight into the prospective materials' feasibility for use in practical DEA applications.

2.4.6 PDMS DEA Load Curves

Section 2.4.4 presented the (nearly) free strain of the actuators, but in order to perform work, an actuator must move a load through a distance. Load curves, which display the work capability of actuators, have not been fully explored in literature. Force, or applied load, is increased along the x-axis and the actuation strain is shown on the y-axis. The intersection of the load curve with the x-axis is the *blocked force*, the load at which the actuator can no longer move through any distance. The intersection of the curve with the y-axis is the *free strain*, which is typically the maximum strain the actuator can achieve. Load curves were created only for PDMS. TC-5005 and VHB-4905 DEAs have too large a creep, which takes place on the time scale of hours (Section 2.4.3). At each loading, the extension was allowed to stabilize for 1 minute, and between measurements the PDMS DEA was given 5 minutes to relax to its original length.

In order to maintain the same electric field, 40 V/μm, throughout testing, the thickness of the elastomer film had to be known. Because direct mechanical measurement would have damaged the electrodes, the thickness under load was determined based on the elongation. The experimentally-determined normalized thicknesses (stretch ratios) of PDMS films without electrodes are shown in Appendix B.2. These thickness estimates were also used to determine the cross-sectional area to calculate the stress from the load. Changes in sample width were neglected. Actuation strains were calculated using the sample length after the load was applied but before

the electric field was turned on (L_0), and the length with the field on after the elongation had stabilized (L).

Figure 2.6 shows the actuation strain for three DEA samples. Two regions can be identified: first, one (0 – 1.8 MPa) where the applied load serves to increase the actuation strain initially before the strain drops under increased load as expected, and a subsequent linear range that ends in a blocked force of 4.4 MPa (1.7 N).
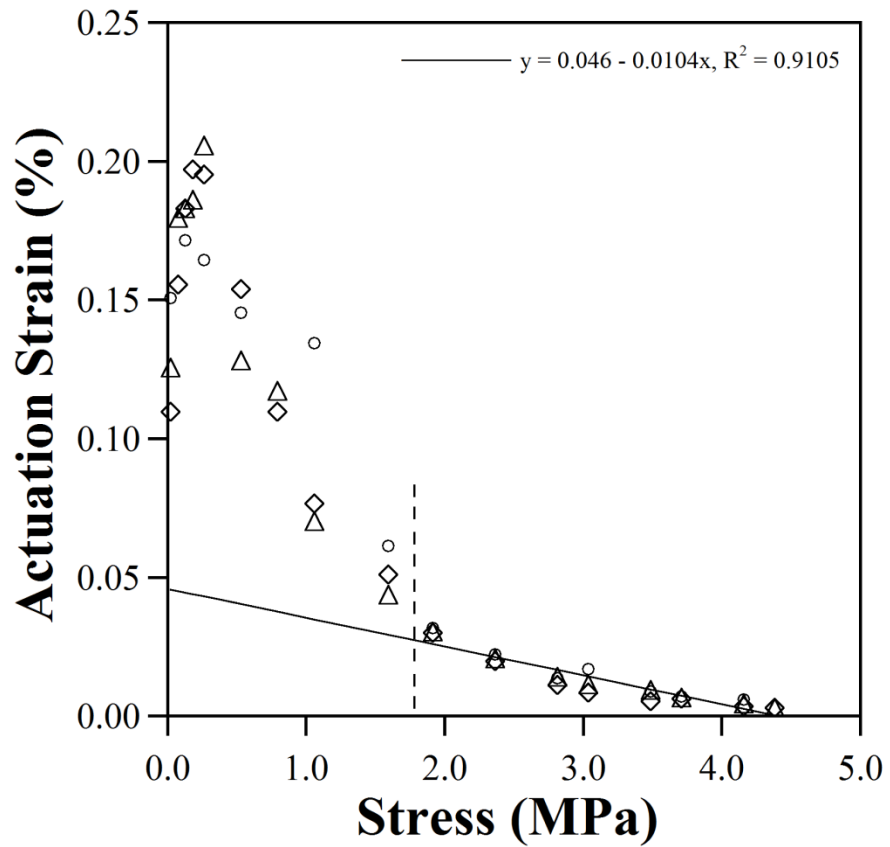
Figure 2.6: Actuation strain as a function of axial load stress for three PDMS-based DEAs under an electric field of 40 V/μm. The solid line represents traditional mechanical actuator behavior and was obtained from a linear fit to the data between 1.8 and 4.4 MPa. The vertical dashed line demarcates two behavioral regions.

The initial increase in the actuation strain in response to increased load has been noted in literature; pre-stress or pre-strain, up to 300% [36], is often applied to increase actuation strain. The reason for this increase to a peak is not clear, but the load-dependent relative dielectric permittivity can be ruled out because it is too small to account for the change and, as has been noted by in literature for the stretched-film DEA configuration, ε_r decreases with pre-strain or axial load [15-17, 19, 20]. We postulate that at low (pre-peak) loads, the actuated area deflects (at least partially) out-of plane upon application of voltage, decreasing the actuation strain observed in-plane. As the loading increases to those corresponding to the peak, this effect decreases, the DEA is constrained to move more in-plane, and the observed actuation strain increases. After the peak, the DEA moves entirely in-plane, and the actuation strain expectedly decreases with increasing load.

2.5 Conclusions

The performance of a DEA was influenced by the elastomer material present in its composition. We examined the key properties of the elastomer material that dictate actuation strain. Although PDMS was an order of magnitude stiffer than TC-5005 and VHB-4905, and exhibited significantly less actuation strain, it had merits; PDMS possessed significantly less creep than the other two materials, allowing for predictable strains and hence, control. In addition, ε_r for PDMS was largely frequency-independent, meaning less attenuation at increased operating frequencies. Although used for the remainder of the work presented in this thesis, PDMS is by no means the best material for DEAs. Such a material would exhibit the better qualities of PDMS but possess a low modulus like TC-5005, with high actuation strain

capabilities similar to VHB-4905. The experimental setup and testing procedure presented in this chapter could serve as a new protocol for future material testing to identify a better DEA elastomer.

The characteristics of the free-film uniaxial (planar) DEA configuration were also observed during testing. The Maxwell model proved too simple to fully describe the behavior of planar DEAs. We postulated that the boundary conditions and the actuator geometry (passive material acting as springs) were at least partially responsible for these discrepancies. The characteristic load curve of the planar DEA was also examined; with its non-linear region where actuation strain initially increases with load before decreasing as expected, and its linear region ending in a measured blocked force of 1.7 N.

Chapter 3: Bending Dielectric Elastomer Actuators

3.1 Authorship & Contributions

The compliant electrode work presented in this chapter (first paragraph of Section 3.5) is adapted from the paper "Elastomers filled with exfoliated graphite as compliant electrodes," Carbon, 48 (9), 2409-2417 (2010), co-written by me, Dr. Mark Kujawski, and Dr. Elisabeth Smela. I am solely responsible for all other work presented in this chapter.

3.2 Introduction

One aim of this research is to enable the further miniaturization of DEA-ambulated robots. As such, it is necessary that the DEA configuration(s) explored be as simple as possible. Along with other more complex configurations, bending DEAs have been explored in the literature [11, 12, 37], although the means of achieving such actuation is quite varied. In this chapter, the conversion of planar DEAs (as detailed in Chapter 2) into bending actuators was investigated and is presented. To begin, it is necessary to propose a potential walking gait (locomotion pattern) for a millimeter-scale, DEA-ambulated robot to serve as a guide for bending DEA design and fabrication.

3.3 Proposed Robot Walking Gait

The walking gait proposed for this project is inspired by the work of Ebefors et. al [5] on their thermally-actuated robot. This gait, as shown in Figure 3.1, is quasi-static, that is, inertial effects on motion are considered negligible.
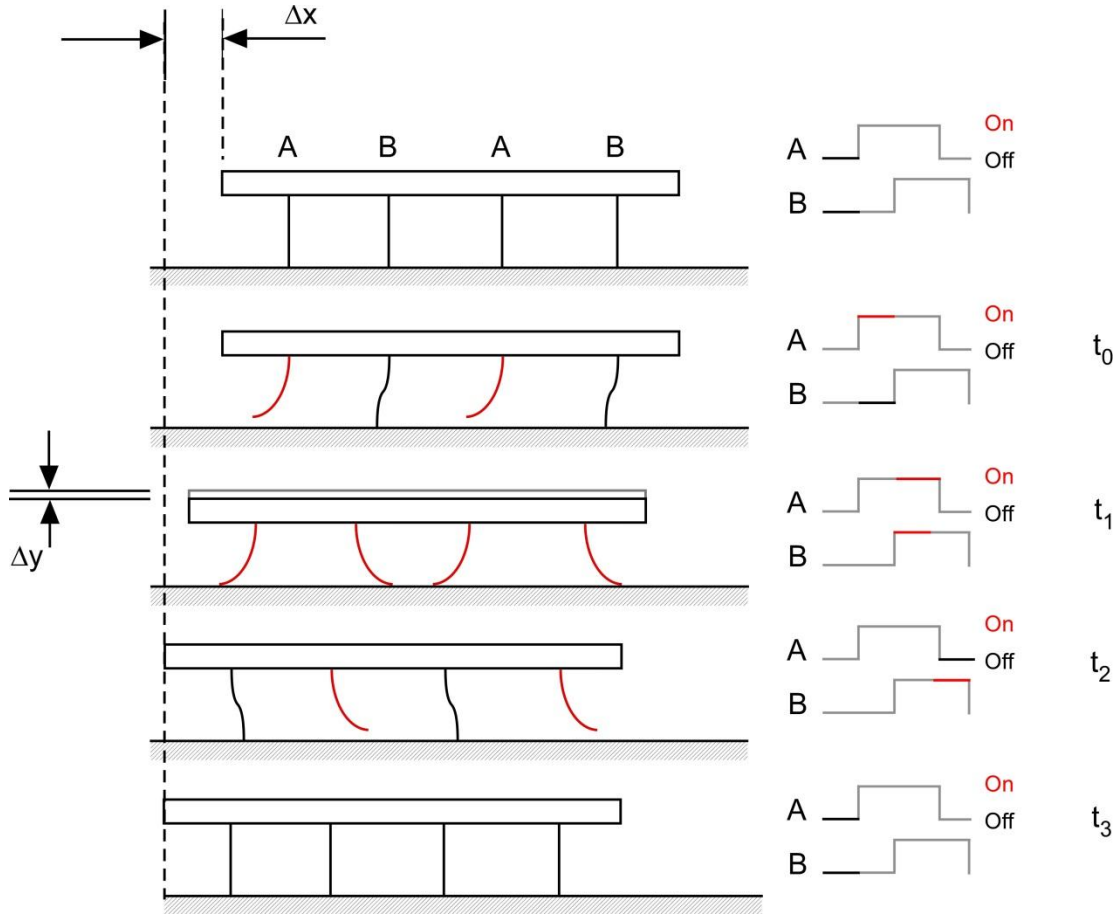
Figure 3.1: Proposed walking gait for DEA-ambulated robot. A no-slip condition on the contact between the DEA leg and the ground is needed to realize the gait in the exact steps presented.

Before the first time step, the robot's weight is supported by all legs which are shared into two groups of four, called A and B. At time t_0, A-designated legs are actuated by applying a voltage, which should cause them to bend upward off the ground. The B-designated legs bow out under the increased weight, but it is assumed that they do not fail due to buckling.

At time t_1 the B legs are actuated and if we assume a no-slip condition on the walking surface, the robot body moves forward (to the left) and downward. The downward

movement Δy is inconsequential as it is restored at the completion of the motion

cycle. Of more importance is the forward motion, which we assume is $\frac{1}{2}\Delta x$ since the

actuator does not undergo its full end displacement because it starts in a partially

buckled (bowed-out) state. We also assume that equilibrium is reached between the

bending actuation force, the restoring force of the elastomer material, and the weight

of the robot so that the robot does not collapse. If this no-slip condition is not present,

the robot will simply drop down, without moving forward.

At time t_2, A-designated legs are un-actuated and as they move to a bowed-out state

on the way back to their original shape, they move the robot body simultaneously

forward by $\frac{1}{2}\Delta x$ and upward by Δy. At the final time step t_3, B-designated legs are

un-actuated and the robot returns to its original configuration, with all legs straight

and a total body displacement of Δx in the forward direction.

For DEAs to act as the legs of robot with such a gait, they must designed to support

load in their axial direction (act as slender beams) and bend out-of-plane (upwards).

In order to achieve the latter requirements, two schema were investigated: the

electrode stiffness differential principle and the asymmetrical surface profile

principle.

3.4 Principles for Achieving Bending DEAs

3.4.1 Electrode Stiffness Differential

In planar DEAs, the electrodes on both sides are typically the same compliant (stretchable) electrodes so that actuation is planar (Figure 3.2a). However, if one electrode was much stiffer ($> 10^3$x) than the other, one would expect that upon electric field application the stiffer electrode should strain less than the elastomer and the less-stiff, more-complaint electrode. If one end of the DEA is fully constrained, the actuator should bend in the direction of the stiffer electrode as shown in Figure 3.2b.

(a)   (b)
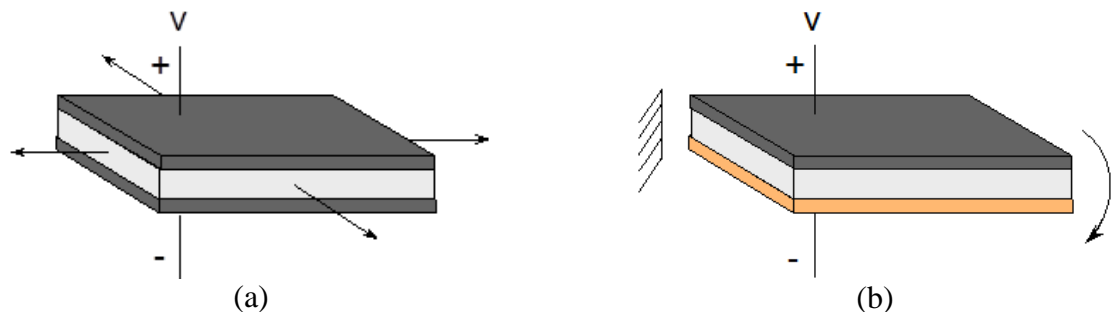
Figure 3.2: (a) DEA planar actuation in response to applied voltage, V. (b) Bending DEA actuation due to stiffness differential between flexible electrode (black) and stiffer electrode (orange). The DEA bends toward stiffer electrode is one end is fixed.

As presented, the stiffness differential bending DEA is a tri-layer. Thus, as the stiffness of the more-compliant electrode starts to approach the modulus of the elastomer layer, the DEA begins to approximate a bilayer.

3.4.2 Asymmetrical Surface Profile

Maleki et al. [37] presented the modeling of bending DEAs with asymmetric surface profiles. As shown in the DEA cross-section (Figure 3.3a), the asymmetry is because of crenellations (raised portions) in the elastomeric layer. Maleki et al. theorized that according to Equation 1.3, if both electrodes are compliant then the force F_2 in the thinner portion of the elastomer (h_1) is higher than the force F_1 in the thicker (crenellated) portion of the elastomer (h_2) when an electric field is applied (Figure 3.3b). This pressure mismatch causes the bottom of the DEA to stretch more than the mid-section, resulting in bending towards the crenellated direction. This effect is assumed to be cumulative so that more crenellations produce more bending.
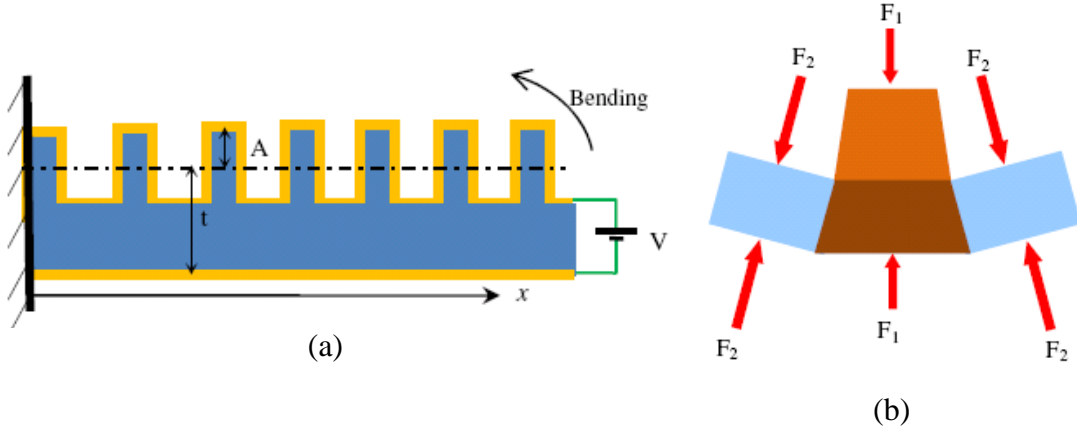
Figure 3.3: (a) Cross section of crenellated DEA with asymmetric surface profile. The elastomer is blue, the electrode is yellow, A is the crenellation amplitude, and t is the distance from the bottom of the elastomer to the mid-point of the crenellations. (b) Cross section showing forces induced by the applied electric field. $F_2 > F_1$ since $h_2 < h_1$, causing bending towards the crenellated side [37].

Other principles for bending have been proposed in literature and in some cases shown to produce bending. For example, Maleki's "unimorph" configuration consists of a planar DEA "active" layer attached to a passive layer of material that does not

strain, causing bending [12]. Multi-layered (stack) DEAs consisting of conjoined unimorphs were developed [38]. Although not examined in the work presented in this thesis, unimorph DEAs could serve as alternatives to the electrode stiffness differential and asymmetric surface profile versions. The stack unimorphs are expected to support more payload due to the amount of material present, but the trade-off with end displacement is likely severe. In addition, the structures are not simple and require numerous processing steps.

3.5   Fabrication

In previous work, we developed and characterized a conductive polymer composite to serve as a compliant electrode for DEAs [39]. The composite, called PDMS/EG, was composed of PDMS mixed with exfoliated graphite (EG). EG is the result of exposing acid-intercalated graphite flakes to high temperatures (> 1000 °C), where upon the acids evaporate rapidly forcefully separating the graphite sheets partially. For the same percent loading in PDMS, PDMS/EG is more conductive than PDMS/graphite. Therefore, less EG is required to achieve a given amount of conductivity than graphite, and thus reduces the adverse effects of conductive material loading on the mechanical properties of the composite. For example, we reported a tangent modulus of 1.44 MPa for 15 % by weight of EG in PDMS (10:1) as compared to 1.06 MPa for pure PDMS [39]. Therefore, a PDMS-based DEA with a PDMS/EG electrode on one end and a much stiffer electrode on the other should behave as a bilayer.

3.5.1 Electrode Stiffness Differential

Bare glass slides (7.5 cm × 2.5 cm) were wiped with acetone, methanol, and isopropanol (in that order) to remove organic material and were dried for 2 minutes at 150 °C. A mixture of 20:1 (resin to curing agent) PDMS was prepared and desiccated for 15 minutes to remove air bubbles. Because 20:1 PDMS is less stiff (0.8 MPa) than 10:1 PDMS (1.06MPa), it is preferred to maximize strain (Equation 1.4), and in turn bending. The PDMS was spin-coated on a glass slide at 750 rpm for 60 seconds to form a 100 μm film. The film was allowed to cure for 30 minutes on a hotplate at 150 °C. After curing, the film was peeled off the glass slide using a razor and then transferred to another glass slide, which served as a carrier. The edges of the PDMS layer were taped to the glass slide, and a vinyl mask (Oracal 651 intermediate cal, Figure 3.4) was applied on top of the layer.
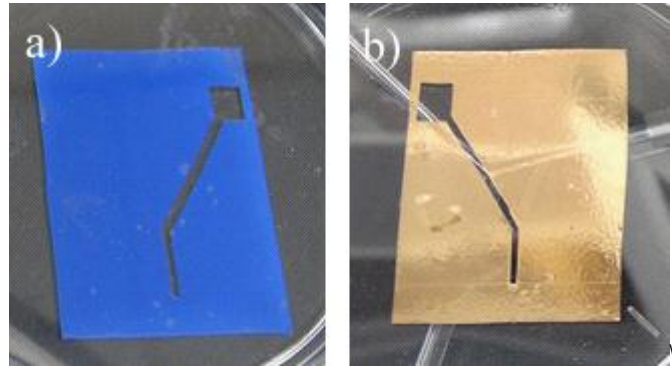
Figure 3.4: Vinyl masks used for electrode deposition. (a) First mask before PDMS/EG electrode deposition. Pattern consists of electrode contact pad and active area connected by a path or trace. (b). Second mask after deposition of the Au electrode.

In order to prepare the compliant electrode (PDMS/EG), 0.05 g of EG was mixed with 6 g of hexane in a glass vial and horn-sonicated (Qsonica) for 1 minute to further

break up the exfoliated carbon (C) sheets. An amount of the hexane (3 g) was evaporated on a hotplate at 150 °C and 0.269 g of PDMS resin was added to form 15 % by weight PDMS/EG. The mixture was bath-sonicated (Branson 1510) for 30 minutes before 0.013 g of PDMS curing agent was added to complete the material. A final bath-sonication for 10 minutes was performed. Using an air-brush (Badger, model 250), the PDMS/EG electrode was sprayed (10 psi) at a distance of 8 cm from the masked PDMS to deposit a 35 ± 5 μm layer. The mask and tape were removed, and the electrode was allowed to cure for 30 minutes at 150 °C.

The stiffer electrode used in this fabrication was gold (Au). After the PDMS/EG electrode was cured, the film was flipped over and secured to a glass slide using tape. A second mask was aligned by eye and applied under a microscope (5x zoom). A 100 nm thick layer of Au was sputtered (Anatech Hummer X sputter coater) on the surface, and the mask was removed to leave the Au electrode. Under a microscope, the now-complete DEA was manually released from the surrounding PDMS with a razor blade. During the release process, a passive PDMS border of approximately 0.5 mm was left on the edges of the actuator to prevent electrical arcing from one electrode to another when high voltage was applied. Recall from Section 2.3.2 that during the fabrication of DEAs with carbon grease electrodes, a passive PDMS border of 2 mm (instead of 0.5 mm) was left on the elastomer's edge. During testing, it became evident that the minimum border length depended on the electrode material, although exactly why this is the case is still unclear. The breakdown voltage of a gas in the presence of an electric field can be estimated using Paschen's law [40].

According to it, the voltage required to cause arcing is 10x higher than that at which arcing was experimentally observed during testing. This indicates that breakdown occurred through some other mechanisms. Based on this hypothesis, thinner borders were used for DEAs with PDMS/EG electrodes and during testing, no arcing between electrodes was observed. It is noteworthy that unlike PDMS/EG, carbon grease may decompose into carbon monoxide, carbon dioxide, and formaldehyde, according to the manufacturer. These gaseous components might play a role in the increased occurrence of arcing in DEAs with carbon grease electrodes.

The portion of the released actuator containing the isolated electrical paths and contact pads for both electrodes was attached to another glass slide using conductive (Ag) epoxy (CW2400, Circuit Works), allowing the DEA active area (bending portion) to hang freely from the end of the glass slide (Figure 3.5). The adhesion between the PDMS and the glass approximates a fully constrained boundary condition on one end of the DEA's active area.
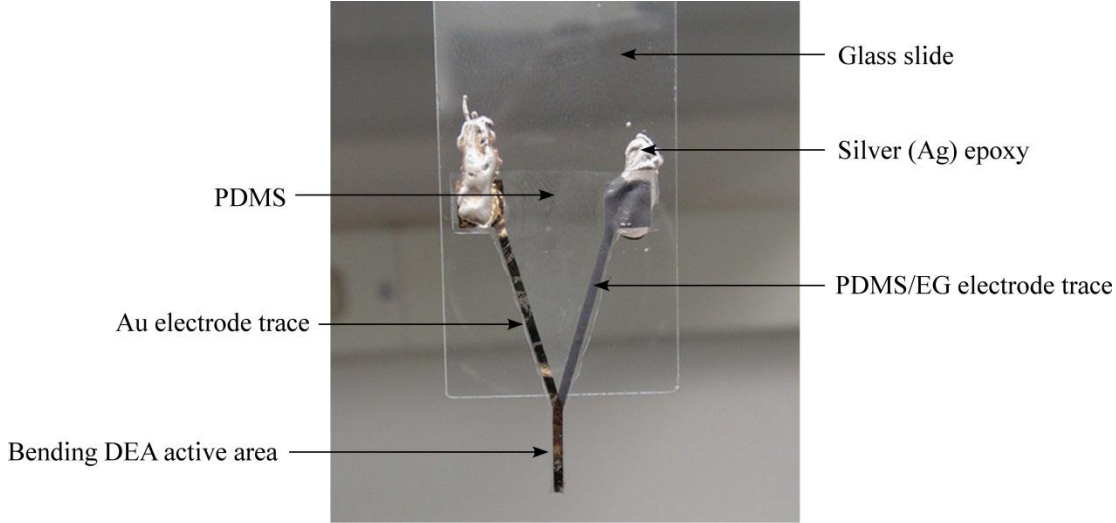
Figure 3.5: Fully fabricated electrode stiffness differential DEA (10 mm × 1 mm wide) attached to a glass slide. The Au and PDMS/EG electrodes are visible in the foreground and background respectively, along with the 0.5 mm PDMS passive border that prevents electricity from arcing across the side of the DEA, from one electrode to another. The Ag epoxies serve as electrical contacts, as well as anchoring the actuator to the glass.

As fabricated, the DEA sample was 10 mm long and 1 mm wide. The portion of the actuator attached to the glass slide is Y-shaped so as to isolate the electrical paths to the electrodes in two dimensions (in-plane and out-of-plane) between PDMS.

3.5.2 Asymmetric Surface Profile

In order to form the crenellated elastomer layer, PDMS was cast on a silicon (Si) mold. The dimensions for the crenellation height and width were selected based on the best results from the simulations presented by Maleki et al. [37]. The photolithography mask created for the mold fabrication contained four different actuator sizes: 5 mm × 0.5 mm, 5 mm × 1 mm, 10 mm × 1 mm, and 10 mm × 2 mm. The length of the crenellation and adjacent flat regions for the 10 mm × 1 mm were 140 μm and 40 μm, respectively. For the other three, the dimensions were 70 μm and 20 μm, respectively. The crenellation height (mold depth) is 100 μm for all four sizes.

The mold was fabricated by dry-etching the crenellations into a 4" diameter Si wafer. 4 μm of photoresist (Shipley 1813) was used as a etch mask in the DRIE process (STS Multiplex ICP). The mold was then surface-modified by treating with a 9:1 volume ratio of methanol and trichloro (1H, 1H, 2H, 2H- perfluorooctyl) silane (Sigma Aldrich) in order to ease the separation between the cast layer and the mold. A finished mold and a close-up of one of the DEA sizes are shown as Figure 3.6.
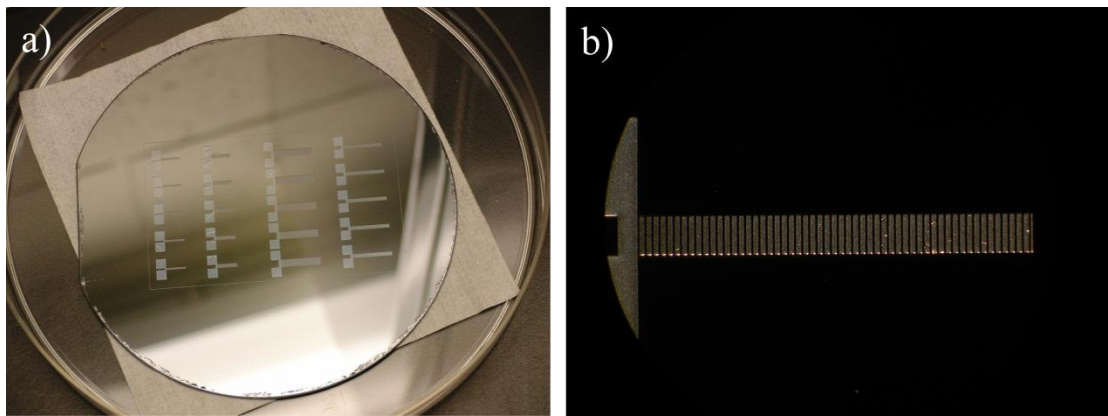
Figure 3.6: (a) Fully fabricated Si wafer mold used to cast crenellated elastomer layers. (b) Close up view of 10 mm × 1 mm actuator showing crenellations.

The DEA configurations shown in Figure 3.6 are T-shaped, unlike the Y-shaped version shown in Figure 3.5. The T-shaped configuration featured electrode contact pad separation in one dimension (in-plane) by 1 mm – 2 mm, depending on the size of the sample length under consideration. During testing, it was observed that when high actuation voltage (>1 kV) was applied, electricity would arc from one electrode to another, shorting the DEA and preventing actuation. This was likely due to the fact that the surrounding air broke down dielectrically and conducted the electricity. The Y-shaped configuration with its bi-dimensional isolation through PDMS was

developed to address this issue. The implications of this decision, in terms of decreased real-estate on the eventual robot body, are further discussed in Chapter 5.

To fabricate the crenellated elastomer layer, 10:1 ratio PDMS was spun unto the surface at 700 rpm and cured at 150 °C to form 100 μm high crenellations on a 100 μm thick base. It is noteworthy that the only size of actuator that regularly survived the cast-mold separation was the 10 mm × 1 mm version, (4th row, Figure 3.6a). All other sizes suffered significantly more defects during the separation process, with portions of crenellations missing as shown in Figure 3.7. It is likely that the thinner gaps between crenellations inhibited PDMS flow into the crenellations during spin-coating. Thus, for the remainder of this thesis, crenellated DEAs are of the 10 mm × 1 mm size only, making them identical to the electrode stiffness differential samples fabricated in the previous section.
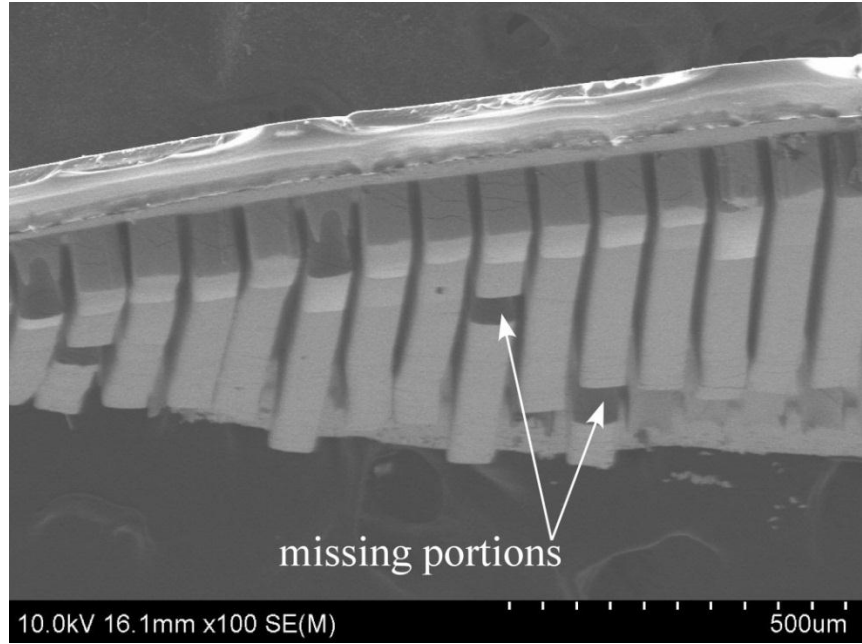
Figure 3.7: SEM photograph of 10 mm × 2 mm crenellated PDMS showing missing portions of crenellations. The 10 mm × 1 mm samples showed these defects significantly less often. Note: sample as pictured is inverted and has Au sputtered on crenellations.

PDMS/EG (35 ± 5 μm) was sprayed on this layer to form one electrode in a process similar to the electrode stiffness differential DEA fabrication. However, it was observed that the PDMS/EG electrode was not conformal when sprayed on the electrodes, as shown in Figure 3.8a. From Figure 3.8b, it is evident that the Au is conformal but its stiffness would hinder bending if it was deposited on both sides of the crenellated elastomer. The solution was to deposit the Au electrode on the crenellated side of the DEA and PDMS/EG on the flat side.

43
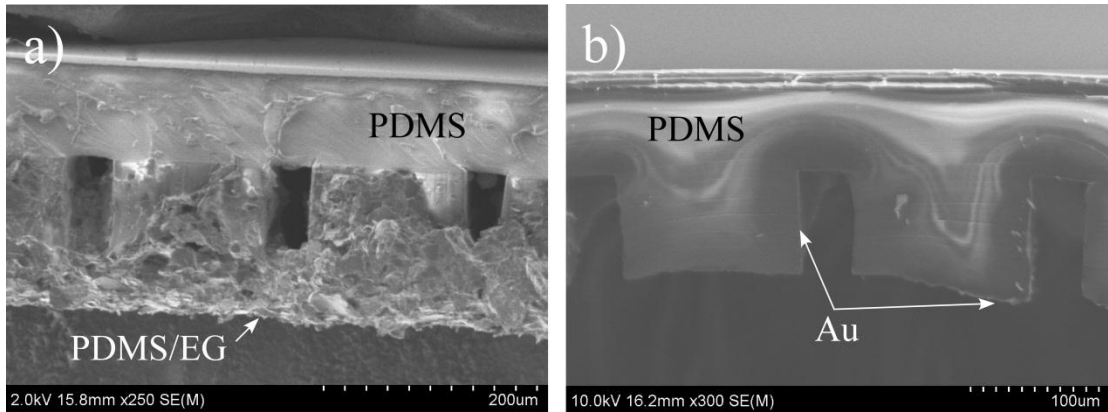
Figure 3.8: (a) SEM photograph of crenellated PDMS cross-section (shown inverted), with non-conformal sprayed PDMS/EG electrodes. (b) Crenellated PDMS cross-section with conformal Au (100 nm) electrodes. The swirls observed on the film are characteristic of insulating materials during SEM and indicate PDMS collecting charge from the electron beam. The thin shiny edge on the crenellations is Au. Both samples shown are 10 mm × 1 mm.

3.6   Experimental, Results & Discussion

Fabricated DEAs of both bending design principles were experimentally tested. For each test, the glass slide supporting the actuator structure was mounted on a stand. The power supply (Ultravolt HV Rack) was attached to the Ag epoxy contacts using small alligator clips. A photograph of the actuator's position was taken at zero applied voltage. Then, the voltage was increased up until a maximum (dielectric breakdown) of 6.4 kV, with the new actuator position photographed at each voltage increment. The photographs were overlaid using software (Canvas X), and the actuator's end displacement was measured (Figure 3.9). The variation in this displacement as a function of the applied voltage is plotted in Figure 3.10. This plot contains data from two 10 mm × 2mm samples: one electrode stiffness differential DEA, and one asymmetrical surface profile DEA.

44
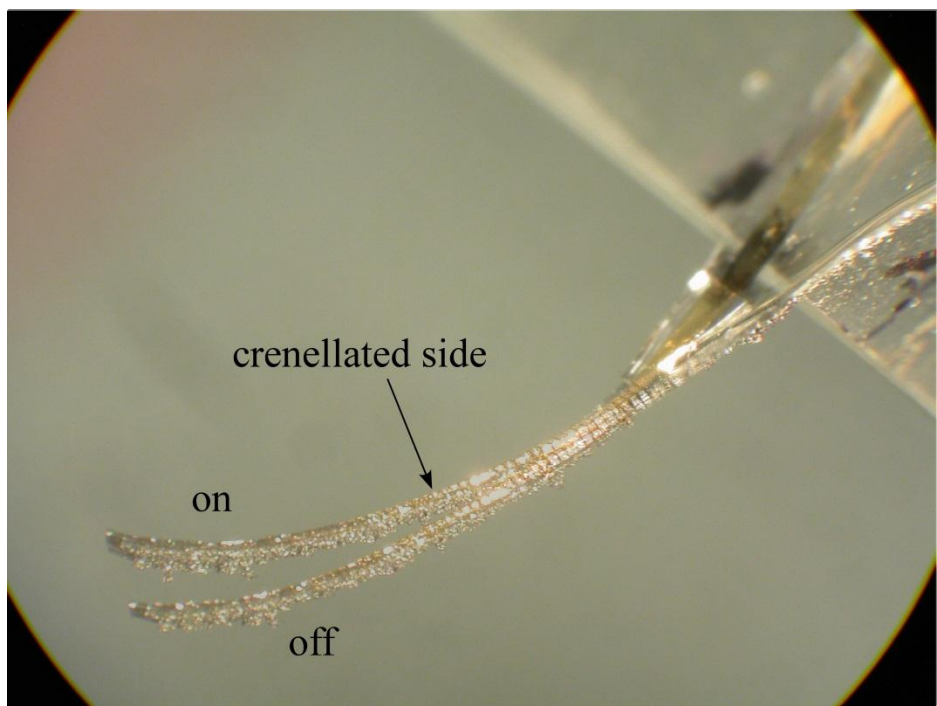
Figure 3.9: Photograph of a 10 mm × 1 mm crenellated DEA sample at rest overlaid with a photograph of the same sample bending under an applied voltage of 5.8 kV (1.3 mm end displacement).
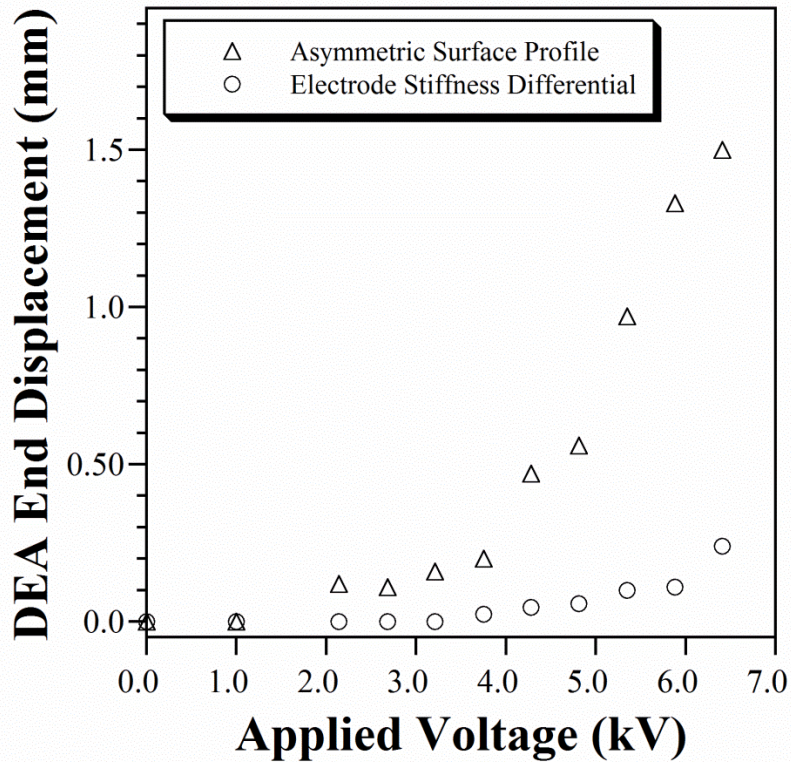
Figure 3.10: Experimental results of bending DEA end displacement as a function of applied voltage for both bending actuation principles: asymmetric surface profile and electrode stiffness differential. Both DEA samples are 10 mm × 1 mm.

As is evident from the figure, the asymmetric surface profile DEAs out-performed

their electrode stiffness differential counterparts by a factor of 10. Both actuator end

displacements followed the increasing voltage-squared trend as expected from

Equation 1.4. At 6.4 kV, the maximum displacements for the electrode stiffness

differential and the asymmetric surface profiler were 0.24 mm and 1.5 mm,

respectively. The best result of the asymmetric surface profile DEA (1.5 mm)

matches well with previously reported results in literature; Araromi et al. [11]

achieved a maximum end displacement of 1.34 mm at 3.8 kV for a 80 mm long, 20

mm wide multi-layer (stack) bending DEA. Maleki et al. [12] achieved a maximum

end displacement of 1.8 mm at 0.45 kV for a 5 mm long, 1 mm wide "unimorph" DEA bender. It is noteworthy that Maleki's DEA features carbon grease electrodes that are impractical for ambulation since they rub off during use.

From the results, it would seem obvious that crenellated DEAs would be better suited as locomotive devices for millimeter-scale robots than non-crenellated DEAs. However, preliminary FEM modeling by Dr. Bavani Balakrisnan in our lab suggested that the mechanisms behind the bending operation of the asymmetric surface profile are more complicated than proposed by Maleki et al. Although important, a thorough understanding of such mechanisms is not the focus of this thesis, and as such will not be detailed here.

3.7   Alternative Uses of Bending DEAs for Robot Ambulation

The walking gait proposed in Section 3.3 highlighted the potential for the use of bending DEAs as legs for millimeter-scale robots. In that circumstance, the DEAs served as both the structural and actuating member of the robot legs. Such an operation is advantageous due to its simplicity in design, fabrication, and ambulatory operation. The disadvantages are limited payload capacity and low force output, both due to the low modulus of the elastomer component of the DEA structure. Perhaps more rigid components could be integrated with the DEAs to serve as supports or structural members, allowing the DEAs to function solely as actuators. Planar fabrication methods have been developed that incorporate rigid composites and compliant flexures to form "knee-like" structures [3]. Bending DEAs could replace these complaint materials in future fabrication. However, for the purposes of this

47

thesis, with its emphasis on simplicity, we only explore the use of bending DEAs as the entire leg structure. Alternative applications might be considered in future work.

3.8 Conclusions

With the proposal of a walking gait for a DEA-ambulated robot, it became apparent that planar actuation of DEAs had to be converted to bending actuation in order to realize robot motion. In order to achieve this goal, two principles (asymmetric surface profile and electrode stiffness differential) were investigated. Bending DEAs were fabricated and realized with the crenellated samples out-performing their non-crenellated counterparts by an order of magnitude. The best result observed was an end displacement of 1.5 mm from a 10 mm long bending DEA. Barring further electro-mechanical modeling and simulations to better understand the asymmetric surface profile principle for bending DEAs, it would seem that this form of actuator is the most promising for use as locomotive devices for millimeter scale robots.

Chapter 4: Performance Optimization of a Millimeter-Sized Robot Ambulated by Dielectric Elastomer Actuators

4.1 Authorship & Contributions

The work presented in this chapter was adapted from a semester project report for ENME 610: Engineering Optimization (Fall 2011). I formulated the optimization problem. The MATLAB code was co-written by me, and the other members of my group, Harish Ganapathy and Haiqing Guo. I performed the data analysis and parametric study.

4.2 Introduction

Before attempting to incorporate the bending actuators (Chapter 3) into a robot, the expected behavior of such a robot was evaluated. To achieve this, the design of electrode stiffness differential bending DEAs was optimized to maximize the performance (speed and payload) of a robot with the walking gait proposed in the previous chapter (Section 3.3). Electrode stiffness differential DEAs were preferred here for their simplicity. For this study, the maximization of both metrics was sought, and thus, they became the subjects of objective functions. It is noteworthy that the simultaneous maximization of these functions results in a conflict: for a given amount of available power, as payload increases, less power is available for movement, and speed decreases in accordance. This conflict was evident in the results presented later in this chapter. The MATLAB script generated for this optimization was robust enough to accommodate more complex modeling in the future.

4.3 Optimization Problem Definition & Formulation

4.3.1 Problem Definition

In order to formulate the optimization problem (maximizing speed and payload), five
major assumptions were made. The first assumption was that the compliant electrode
had the same stiffness as the elastomer. If we assume the elastomer is
polydimethlysiloxane (PDMS, Dow Corning Sylgard 184), then the electrode could
be PDMS/EG, with a tangent modulus (stiffness) similar to that of PDMS [39]. This
assumption allowed for the incorporation of the electrode into the PDMS layer, and
converted the tri-layer DEA into a bilayer. The second assumption was that this
subsequent bilayer could be modeled by an adaptation of the Timoshenko bilayer
bending equation.

The third assumption was that the maximum voltage PDMS could withstand before it
suffered dielectric breakdown (allows current flow), V_{max} was independent of its
resin-to-curing agent mixture ratio. Since this ratio allowed the elastomer modulus,
E_2 to vary, this assumption decoupled these two variables. The fourth assumption was
that the DEA legs could be modeled as non-ideal columns where there was some
eccentricity e, a small offset between the centroid of the column and the line of force
on the payload that allowed the beam to experience a small deflection before
buckling failure. Otherwise, the DEA leg does not deflect by δ, but instead, remains
straight until an immediate catastrophic failure at the critical load. The columnar legs
were fixed-pinned at the boundaries so that in supporting payload the attachment of

the leg to the robot body was modeled as a fixed constraint while the leg's contact to the floor was modeled as a pinned, no-slip constraint.

The fifth assumption was that the DEA strain, and subsequently the actuator end displacement, was not significantly attenuated by increased frequency. This was not truly the case so this assumption was a simplification of the physical occurrences.

4.3.2 Formulation

The speed u of the robot is the product of the actuator step size Δx and the frequency of the applied voltage f. Therefore, the objective function for speed is given as

$$u = \Delta x \times f \tag{4.1}$$

The step size is obtained from an approximation based on the curvature of the bent DEA, ρ. This "arc length" approximation is given as

$$\Delta x = \rho \left[1 - \cos\left(\frac{L}{\rho}\right) \right] \tag{4.2}$$

where L is the length of the DEA. It is noteworthy that Equation 4.2 provides a physics-based constraint on the speed. This is accomplished through the $\cos(L/\rho)$ term, which limits the bending of the DEA leg because the length decreases significantly compared to the radius of curvature.

As discussed in Chapter 1, the in-plane strain exhibited by DEAs upon voltage application is commonly given by Equation 1.4. But as shown in Figure 2.5a, the model over-predicted the actuation strain of the planar DEA (by 47x for PDMS). As summarized in that section, it has been noted in literature that the boundary conditions and the device configuration are, at least in part, responsible for these discrepancies, although the exact extent is still unclear. Thus, many researchers have sought to use modified versions of this Maxwell model and other models entirely. One such modification to the Maxwell model involves halving it [10, 14, 21, 34]so that the out-of-plane stress is given by

$$\sigma = \frac{1}{2}\varepsilon_0\varepsilon_r\left(\frac{V}{h}\right)^2 \qquad (4.3)$$

This form of the Maxwell electrostatic pressure equation is "conservative", and because it is simple, allows for easy modification to the code as necessary. Therefore, it is used for the DEA modeling in this chapter.

Consolidating the Timoshenko bilayer equation [41] with Equation 4.3, we have that the curvature κ of the bending DEA is given by

$$\kappa = \frac{1}{\rho} = \frac{\upsilon\varepsilon_0\varepsilon_r\left(\frac{V}{h_2}\right)^2}{2E_2h_2} \times \frac{6mn(1+m)}{1+4mn+6m^2n+4m^3n+m^4n^2} \qquad (4.4)$$

where v is the Poisson's ratio of PDMS, E_2 is the tangent modulus of the combined compliant electrode/ elastomer layer, h_2 is the thickness of that layer, and m and n are the ratio of the layer thicknesses and moduli, respectively, and are given by

$$m = \frac{h_1}{h_2} \,,\, n = \frac{E_1}{E_2} \qquad\qquad (4.5, 4.6)$$

where, h_1 is the thickness of the stiffer electrode layer.

To formulate the objective function for payload per leg, P, we begin by modeling the DEA as a slender load-bearing column. From beam theory, for the ideal fixed-pinned column shown in Figure 4.1, the sum of moments about the origin at equilibrium gives

$$EIv'' + Pv = 0 \qquad\qquad (4.7)$$
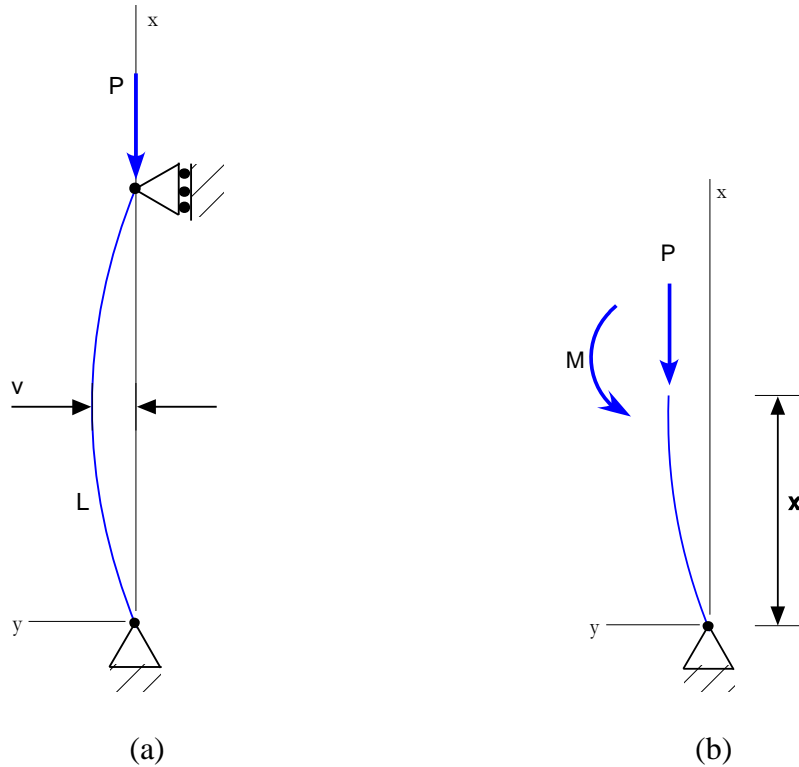
Figure 4.1: (a) Ideal fixed-pinned column, (b) showing moment caused by payload.

where I is the moment of inertia of the DEA structure and is given by

$$I = \frac{b(h_1 + h_2)^3}{12} \tag{4.8}$$

where b is the width of the DEA leg. Modeling the DEA as a non-ideal fixed-pinned column as shown in Figure 4.2, the equilibrium equation becomes

$$M = EI\delta'' = Pe - P\delta \tag{4.9}$$

Thus, the deflection δ before buckling failure is given by [42]

$$\delta = e \left[\sec \left(\frac{\pi}{2} \sqrt{\frac{P}{P_{cr}}} \right) - 1 \right] \qquad (4.10)$$

where the critical buckling load, P_{cr} is [42]

$$P_{cr} = \frac{2.046\pi^2 EI}{L^2} \qquad (4.11)$$

It is noteworthy that P_{cr} is a physics-based constraint on the payload per leg because

for $P \geq P_{cr}$ buckling failure occurs.
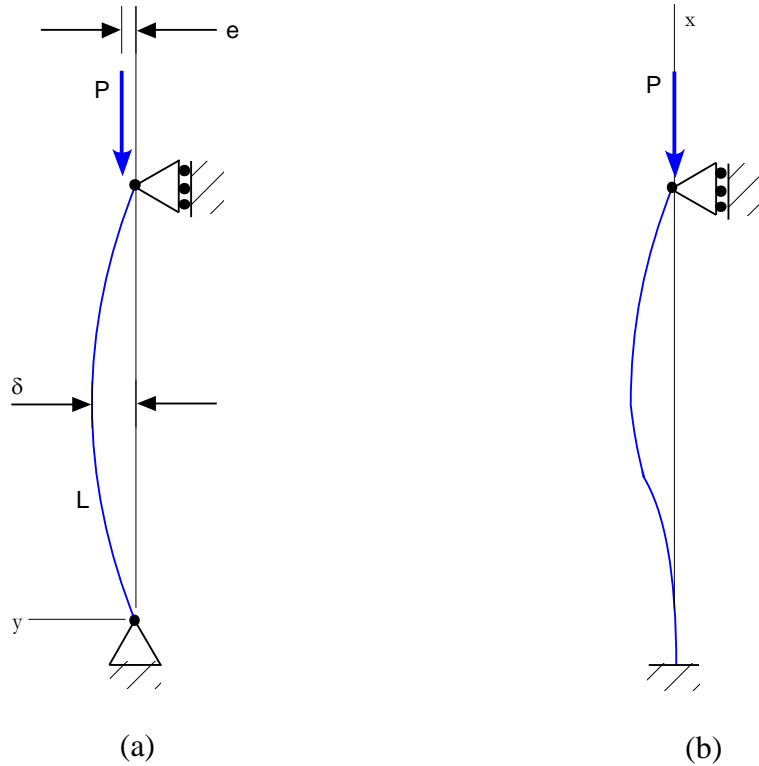
Figure 4.2: (a) Non-ideal fixed-pinned column model for DEA legs (b) Actual deflection shape.

Therefore, rearranging Equation 4.10, the objective function for the payload per leg is given as

$$P = P_{cr} \left[\frac{2}{\pi} sec^{-1} \left(\frac{\delta}{e} + 1 \right) \right]^2 \qquad (4.12)$$

The variables for this optimization problem were the thickness of the stiffer electrode (Au in this case), h_1, the elastomer/ compliant electrode thickness, h_2, the DEA length, L, the elastomer modulus, E_2, the voltage frequency and amplitude, f and V, respectively, and the non-idealization ratio (δ/e) (abbreviated as ni in the MATLAB code). Constraints for h_1 and h_2 were based on layer deposition limits. L was constrained by reasonable physical considerations for a millimeter-scale robot. E_2 was constrained by the requirements for the curing of the PDMS resin. f was constrained by the material time response (the amount of time it takes the material to respond and/or relax) of the PDMS, which is approximately 10 ms. The maximum voltage was constrained by the breakdown voltage of PDMS. The non-idealization ratio was approximated from the literature [42]. The fixed parameters were the modulus of the stiffer electrode, E_1, and the width of the DEA leg, b, whose influence on the solution to the optimization problem are explored later in the chapter. The variables, their symbols, and lower and upper limits used for the design optimization problem are shown in Table 4.1.

Table 4.1: Design variables for the multi-objective optimization problem.

No.	Variables	Lower Limit	Upper Limit	Determines
1.	Au layer thickness (h_1)	10^{-8} m	10^{-6} m	Payload and Speed
2.	PDMS layer thickness (h_2)	10^{-5} m	10^{-3} m	
3.	Length of DEA leg (L)	10^{-3} m	10^{-2} m	
4.	Tangent modulus of PDMS (E_2)	0.8 MPa	1.8 MPa	
5.	DC voltage frequency (f)	10^{-1} Hz	100 Hz	Speed
6.	Voltage amplitude (V)	0 V	6400 V	
7.	Non-idealization (δ/e) ratio	0.1	0.5	Payload

Therefore, the complete performance optimization as presented in standard problem statement form is:

maximize $\quad u = \Delta x \times f$

$$P = P_{cr} \left[\frac{2}{\pi} sec^{-1} \left(\frac{\delta}{e} + 1 \right) \right]^2$$

subject to $\quad g1: 10^{-8} \leq h_1 \leq 10^{-6}$

$\quad\quad\quad\quad g2: 10^{-5} \leq h_2 \leq 10^{-3}$

$\quad\quad\quad\quad g3: 10^{-3} \leq L \leq 10^{-2}$

$\quad\quad\quad\quad g4: 0.8 \leq E_2 \leq 1.8$

$\quad\quad\quad\quad g5: 10^{-1} \leq f \leq 10^2$

$\quad\quad\quad\quad g6: 0 \leq V \leq 6400$

$\quad\quad\quad\quad g7: 0.1 \leq ni \, (\delta/e) \leq 0.5$

$$g8: P \leq P_{cr} = \frac{2.046\pi^2 EI}{L^2}$$

$$h1: \Delta x = \rho \left[1 - \cos\left(\frac{L}{\rho}\right) \right]$$

where g's are inequality constraints and h_1 is an equality constraint.

For the formulation of objective functions for speed and payload, the models of the DEA legs developed here feature the use of a bending DEA as the entire leg structure. As discussed in Section 3.7, one may consider alternative versions of legs where the DEAs act as "knees", bending rigid components. Since P_{cr} is inversely proportional to L^2 (Equation 4.11), this would increase the payload capacity of the leg. If that were to occur, the modeling performed here would need to be modified to account for the added components. Thus, these models are incomplete for the time being.

4.4 Methods, Results & Discussion

4.4.1 Multi-Objective Optimization

The multi-objective problem was solved using a canned approach (*fminimax*) solver in MATLAB: the code is reported in Appendix C. For convenience, the initial values of the variables were selected to be midpoints of the upper and lower bounds of the variables as defined in Table 4.1. These initial values as well as the optimized values of the variables are tabulated in Table 4.2. The results indicated that the a millimeter-scale robot operating with these optimal values would have a payload per leg capacity of 110 mg and a speed of 6.88 mm/s.

Table 4.2: Results of multi-objective optimization for speed and payload per leg by canned approach.

Variables	Initial Value	Optimized Value
h_1 (m)	5.05E-07	1.00E-08
h_2 (m)	5.05E-04	1.26E-04
L (m)	5.50E-03	2.82E-03
E_2 (Pa)	1.30E+06	1.30E+06
f (Hz)	5.01E+01	5.06E+01
V (Volts)	3.20E+03	3.20E+03
δ/e (-)	3.00E-01	3.27E-01
Speed (mm/s)	0.42	6.88
Payload (g)	1.81	0.11

Ebefors et al. developed a thermally actuated walking robot that featured a payload per leg capability of 312.5 mg (2500 mg total for 8 legs) and a speed of 6 mm/s [5]. It is interesting that both those values compare well with the results of this study. As discussed in Section 1.2, it is expected that Ebefors' legs (Si) are stronger (3x, based on these results) than the proposed DEA legs. The optimum material dimensions are all feasible and can be deposited easily. The applied voltage magnitude is still large (kV range) so a tether to a power supply is still required. The voltage frequency is manageable and should not cause significant attenuation. The non-idealization ratio is within the reasonable limits.

4.4.2 Parametric Studies

The parametric study is an analysis of the sensitivity of the optimization results to changes in the fixed parameters. As presented in this thesis, the two parameters are E_1

and b. These studies were executed by performing the multi-objective optimization presented in the previous section while varying the value of the fixed parameter. It is noteworthy that for each value of a parameter, a new feasible domain (set of optimization solutions) was established with its own local and global maxima.

4.4.2.1 Non-Compliant Electrode Stiffness (E_1)

The first parameter tested was E_1. For the multi-objective optimization, the value used was 80 GPa (Au). In the parametric study, E_1 was varied from 70 GPa (Aluminum) to 280 GPa (Chromium). The optimum speed and payload as functions of the stiffness of the non-compliant electrode are plotted in Figure 4.3a and b.
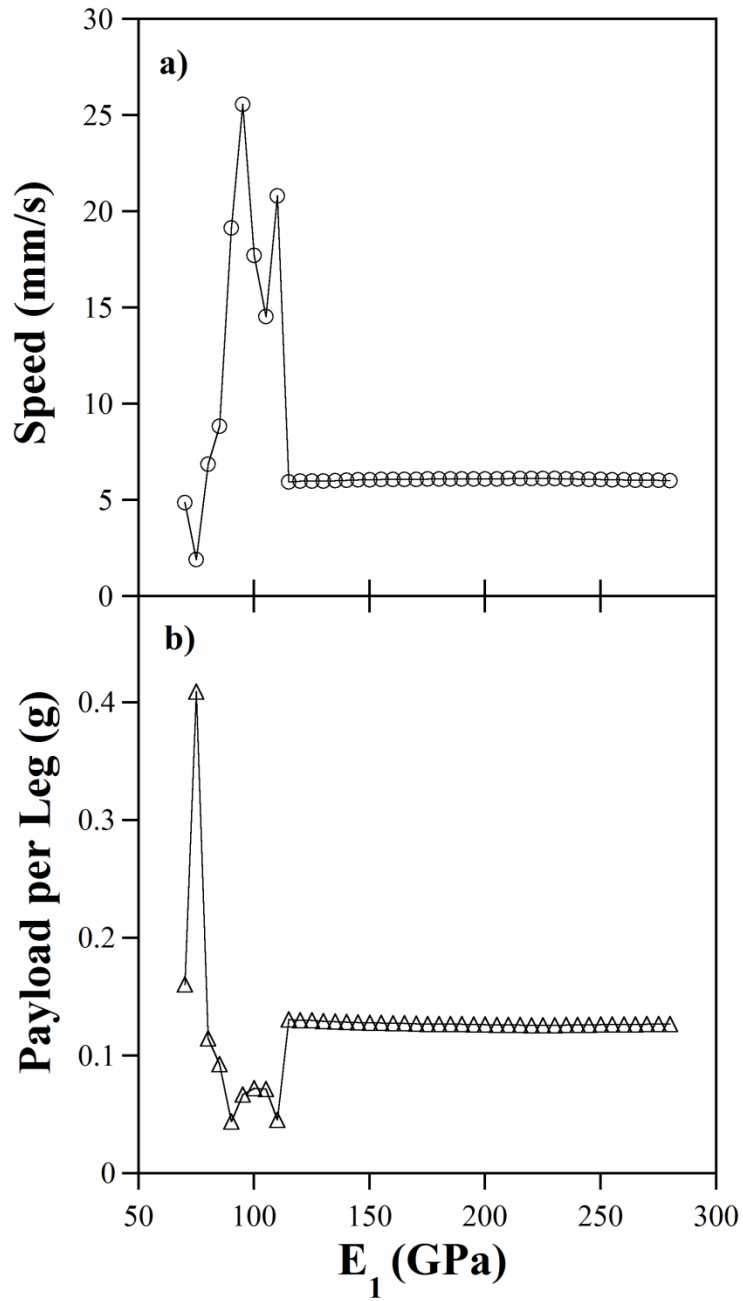
Figure 4.3: The effect of variance in the parameter E_1 (non-compliant electrode stiffness) on the optimization results for (a) speed and (b) payload per leg. The solid lines are guides for the reader.

From Figure 4.3, it can be seen that between 70 GPa and 115 GPa, changes in E_1 result in large fluctuations in both the optimum speed and payload, following no discernible trend. The reason(s) for this behavior is not clear. It may, however, be of

61

little concern since realistically, the modulus of metals in this range are discrete; consider complications borne from the need to deposit these materials in thin (μm) layers. The opposing nature of the objective functions is confirmed by the results shown in the figure. After 115 GPa, the optimization solution becomes insensitive to increases in E_1, maintaining the same optimum result of 6.01 mm/s and 127 mg. In other words, for each feasible domain created by a different value of the fixed parameter, the optimization result returns to the same global maximum by shifting around values for variables within the specified limits. It is interesting that this result matches well with the optimum derived in the previous section with Au as the non-compliant electrode.

4.4.2.2   Width of DEA Leg (b)

The second parameter examined was b. For the multi-objective optimization, the value used was 1 mm. In the parametric study, b was varied between 0.5 and 2 mm. The results from the parametric study are presented in Figure 4.4.
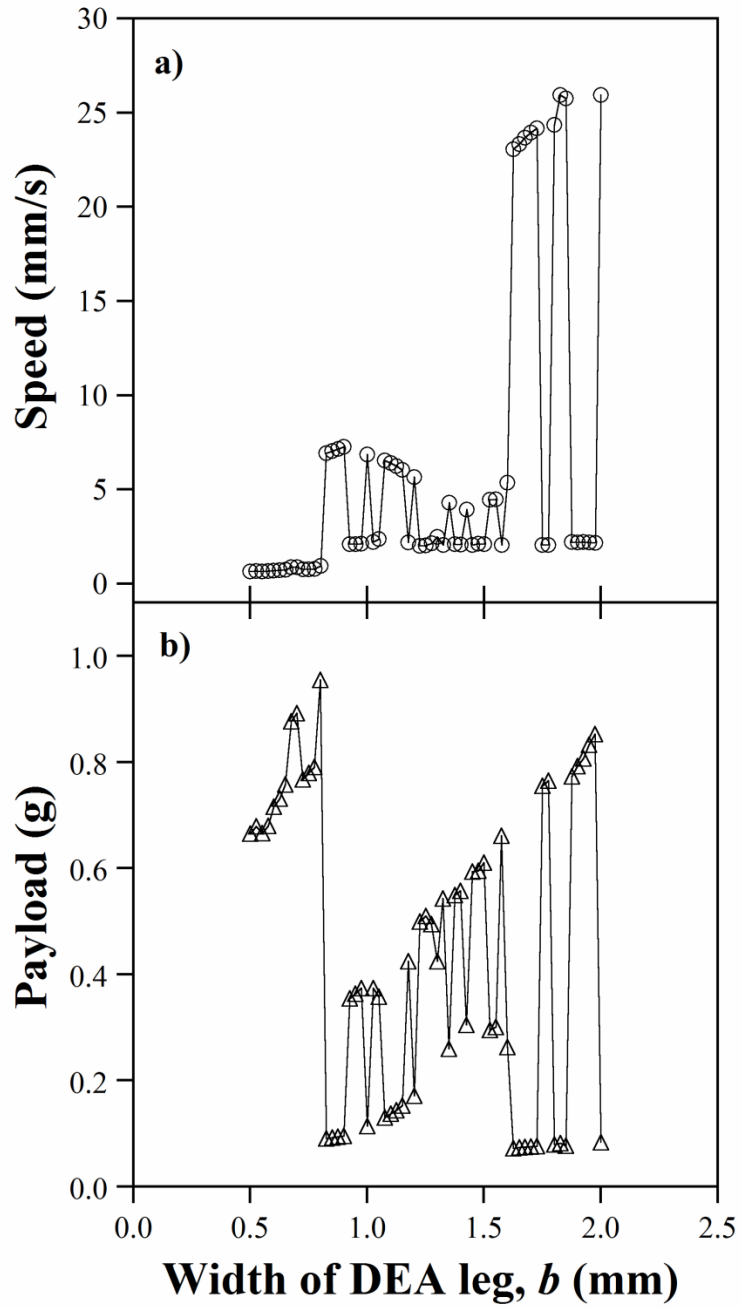
Figure 4.4: The effects of variance in the parameter *b* (width of DEA leg) on the optimization results for (a). Speed, and (b). Payload per leg. The solid lines are guides for the reader.

From the Figure 4.4, the inverse relationship between optimum speed and payload was observable. Also, the optimization results did not follow any discernible trend but rather, as the optimization selected the values for the variables to maximize

performance while accounting for the change in b, the results seemed to move between local and global maxima. In other words, for each feasible domain created by a different value of the fixed parameter, the optimization result occurs at a maximum that could be global or local in that domain but differs from domain to domain with the value of the parameter in no predictable way. The apparent sensitivity of the optimization results to changes in b is an indication of the importance of properly selecting this parameter.

4.5   Conclusions

In this chapter, the optimization of DEA legs for a millimeter-scale robot was sought. Based on a proposed walking gait along with several assumptions, the DEA leg structure was modeled as a slender load-bearing column while its actuation was modeled using bilayer bending theory. With these models established, the objective functions for speed and payload to be maximized for increased performance were formulated. The optimal design was obtained using *fmiminax* to solve the multi-objective problem. The achieved optimal value was 6.88 mm/s for speed and 110 mg for payload per leg. These results match closely to a previously reported thermally actuated walking robot with a speed of 6 mm/s and a payload per leg of 312.5 mg. The optimized dimensions are all feasible and can be readily deposited and fabricated. Within certain limits, the optimization results seem to be sensitive to changes in the fixed parameters E_1 and b, and so caution should be exercised in selecting these parameters. Although the results from this optimization provide useful insight into design choices and estimates for performance, improvements remain be made to the model and optimization formulation.

Chapter 5: Challenges to the Realization of Millimeter-Scale Robots Ambulated by Dielectric Elastomer Actuators

5.1 Authorship & Contributions

I am solely responsible for all the work presented in this chapter.

5.2 Introduction

In the previous chapters of this thesis, the characterization of planar (uniaxial free-film) DEAs was undertaken and the performance of PDMS as the elastomeric base of such actuators was examined. Following this, in-plane strain was harnessed to produce bending actuation as required to realize a robot with the proposed walking gait. The performance of DEA legs were optimized in order to gain some insight into potentially achievable results with a DEA-ambulated robot. The next step would be to attach these fabricated bending DEA legs to a robot "body" and attempt to achieve some ambulation. Several challenges were encountered that seriously threaten this realization. Some of these challenges are discussed in this chapter, namely issues associated with the DEAs' interactions with their surroundings, and the attachment of these actuators to a robot body to form legs.

5.3 DEA Interactions

The high voltage required to induce appreciable actuation from DEAs is problematic for autonomy because the robot would have to be tethered to an external power supply. However, in addition to this, the high voltage applied over thin dielectric layers results in high electric fields that cause the DEA to electrostatically interact with the surrounding media. This media includes adjacent DEAs, the bottom of the

65

robot body, inanimate objects around the DEA, and the surface on which the robot is ambulating.

A series of simple experiments to illustrate these interaction effects were performed. Using the electrode stiffness differential DEA (Chapter 3), two samples were arranged in three configurations. For all three configurations, the samples were placed so that the glass slides supporting them were 12 mm apart (glass slide is 1 mm thick). In configuration 1 (Figure 5.1a), the samples were oriented so that both samples are expected to, independent of one another, bend in the same direction. In this configuration, the distance between the tips of the actuators was 21 mm. Upon voltage application (4 kV or 40 V/µm) to the two actuators, the left-most sample bends in the expected direction while the right-most sample was forced in the opposite direction from that expected, as shown in Figure 5.1b. The distance between the actuator tips increased to 24 mm. This illustrated the "repulsive" DEA interaction.
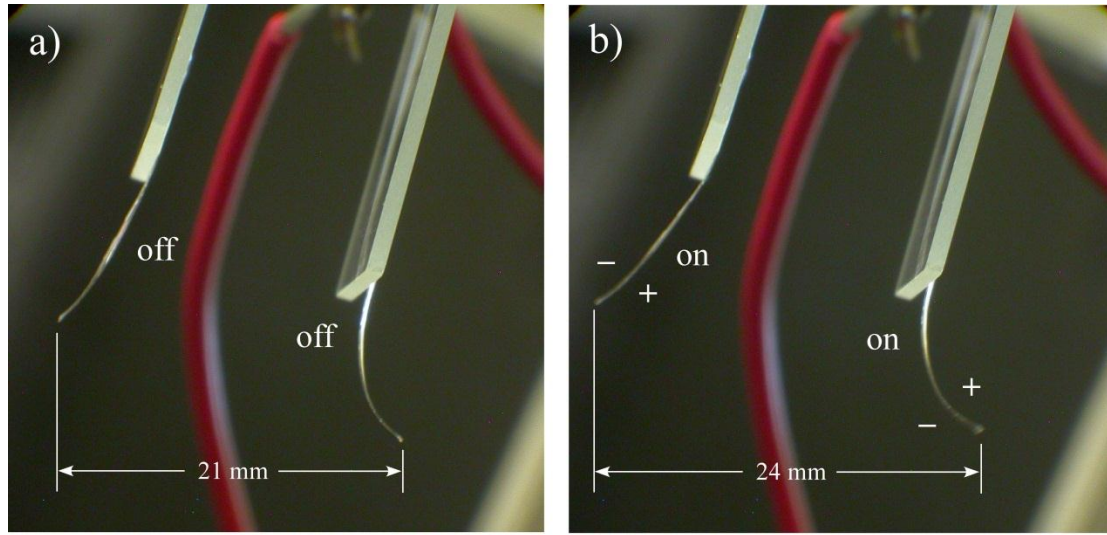
Figure 5.1: DEA interaction testing in configuration 1 (DEAs arranged so as to bend in the same direction). (a) Samples at rest with no voltage applied. The curvature of the samples at rest is due to residual stress imparted during the fabrication and release process. (b) Samples repulsing each other upon simultaneous voltage application (4 kV).

In configuration 2, the actuators were arranged so that in the absence of interaction effects, they would bend toward each other (Figure 5.2a). When both actuators were switched "on", the repulsive interaction was also observed (Figure 5.2b). Based on the results of configuration 2 alone, one could postulate that the observed repulsion was due to the presence of like charges on the electrically positive (Au) face of the actuators. However, this theory does not explain the repulsive behavior observed for configuration 1 where one would have expected the interaction to be of the "attractive" kind since the positive (Au) face of one sample was adjacent to the negative (PDMS/EG) face of the other.
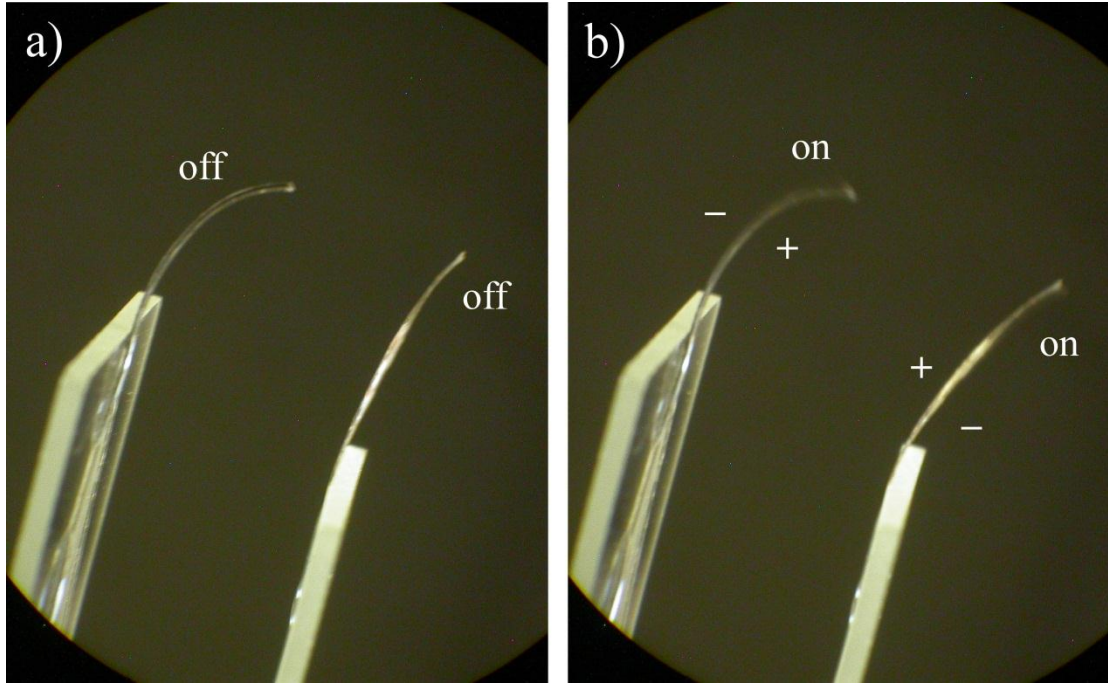
Figure 5.2: DEA interaction testing in configuration 2 (DEAs arranged so as to bend towards each other). (a) Samples at rest with no voltage applied. (b) Samples repulsing each other upon simultaneous voltage application (4 kV).

From the repulsive interactions noted as the result of testing in both configurations 1 and 2, it seems that simple charge interactions play, at the most, a diminished role in the causation of these interaction effects. The dominant cause of these effects is likely fringe or stray capacitance caused by the high electric fields.

In addition to repulsion, another interaction effect between DEAs was noted in the form of attraction. This was best illustrated by testing in configuration 3 where the two samples were arranged so that only one would be actuated by voltage, bending towards the direction of its non-actuated neighbor. The results are shown in Figure 5.3.
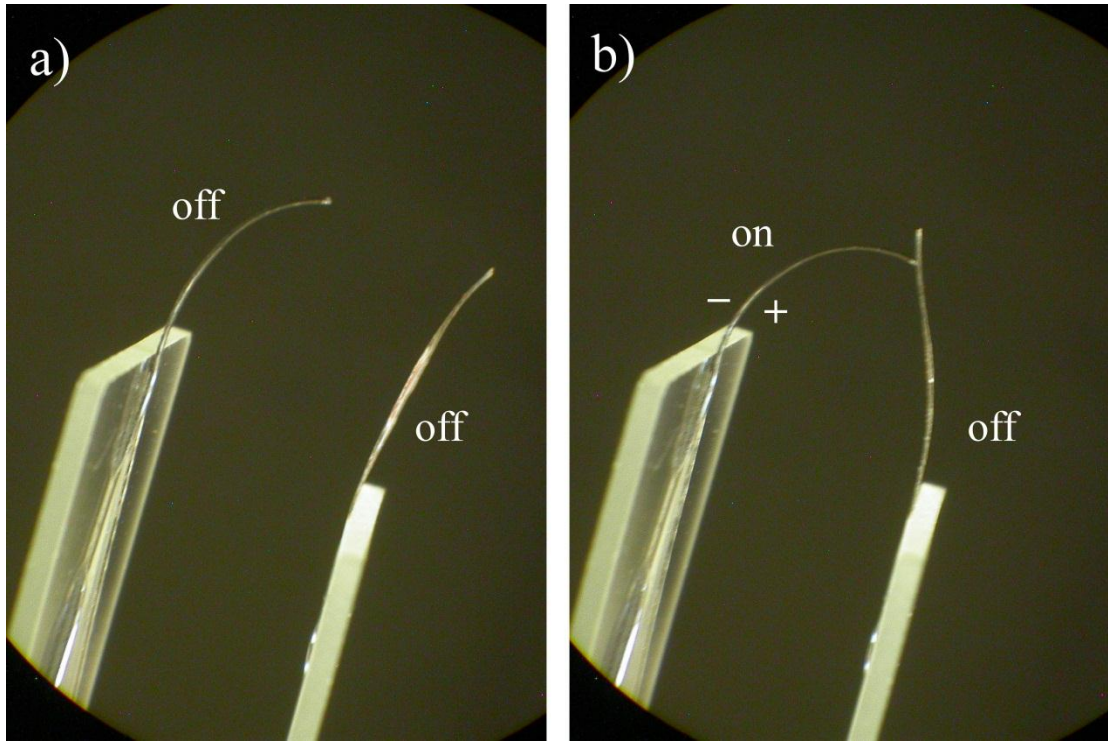
Figure 5.3: DEA interaction testing in configuration 3 (DEAs arranged so that only one sample is actuated and bends towards the other, which is at rest). (a) Both samples at rest with no voltage applied. (b) Only the left-most sample is actuated (4 kV) and bends toward the one at rest, eventually contacting and sticking to it.

Initially, both samples were adjacent and at rest (Figure 5.3a). The left-most DEA

was then actuated with 4 kV, bending toward the right-most DEA, the expected

direction. However, as this highly charged actuator bended, it pulled the un-actuated

DEA towards it until contact was made. Sometimes, as shown in Figure 5.3b, the

actuators stuck together. Other times, the actuators repelled immediately after contact.

The former occurrence is possibly due to PDMS passive borders sticking to one

another, while the latter is caused by charge dumping, equilibrium, and like-charge

repulsion upon contact between the DEAs. Indeed, this attractive form of interaction

has been observed by the author when objects are brought in close proximity of "on"

bending DEAs. This is because relative to the DEA (experiencing a strong electric field), most objects are grounded, and thus an attractive effect is induced.

Other interactions may occur such as charge loss when a bending DEA leg with exposed electrodes contacts a conductive surface during ambulation. This charge loss would effectively un-actuate the DEA leg, inhibiting the locomotion. The use of passive insulating layers over the electrodes would address this issue but such additions would increase the weight of the DEA leg, and reduce the maximum displacements.

DEA interactions are a serious roadblock to the use of DEAs as millimeter-scale robot legs since such applications entail close proximity between the actuators, as well as contact with a myriad of surfaces. The likely solution is the weakening of the actuating electric field through intelligent design. For example, an increase in DEA elastomer thickness (or alternatively, a decrease in applied voltage magnitude) will reduce the magnitude of the electric field and along with it, the severity of interactions. However, actuation strain is also reduced (Equation 1.4). Or possibly, the robot may be designed so that portions of it use the DEA interactions to its advantage; for example, using repulsion towards a certain direction to improve bending performance in that direction. Perhaps, the solution lies with the employment of better materials: ones that exhibit higher strains at lower electric fields. Either way, further insight must be gained from more thorough interaction effects testing.

5.4 Mechanical & Electrical Attachments of DEA Legs to Robot Body

In order for the DEAs to perform their intended function as legs, they must be both mechanically and electrically attached to some form of robot body. Inevitably, the robot body must be lightweight to maximize payload capacity and must facilitate the attachment of DEAs. With regards to the bending DEAs used in this work, the simplest form of robot body, therefore, is a thin slab of PDMS. Robot mock-ups were fabricated.

As shown in Figure 5.4a, the first mock-up was made entirely of 20:1 ratio by weight PDMS and composed of a 3.5 cm × 2 cm × 0.1 cm slab for a body and 1 cm × 0.2 cm × 0.1 cm legs (17 total). The legs were attached to the body by PDMS that is cured at 60°C overnight in an oven, effectively serving as glue. As demonstrated in the figure, the mock-up was able to stand under its own weight, similar to how the robot in the proposed walking gait (Section 3.3) was envisioned to remain at rest. Another mock-up (shown inverted in Figure 5.4b) was fabricated to determine the feasibility of the proposed design using legs similar in shape to the bending DEAs developed in Chapter 3. For this, the shapes of 5 mm × 1 mm actuators (T-shaped) were cut from a 200 μm 20:1 ratio PDMS layer using laser machining (Appendix D) and attached to the underside of a 4.5 cm × 1.5 cm × 0.1 cm slab, which acted as the robot body. There were 8 legs in total, arranged in two groups of A-and B-designated legs as originally proposed in Chapter 3.
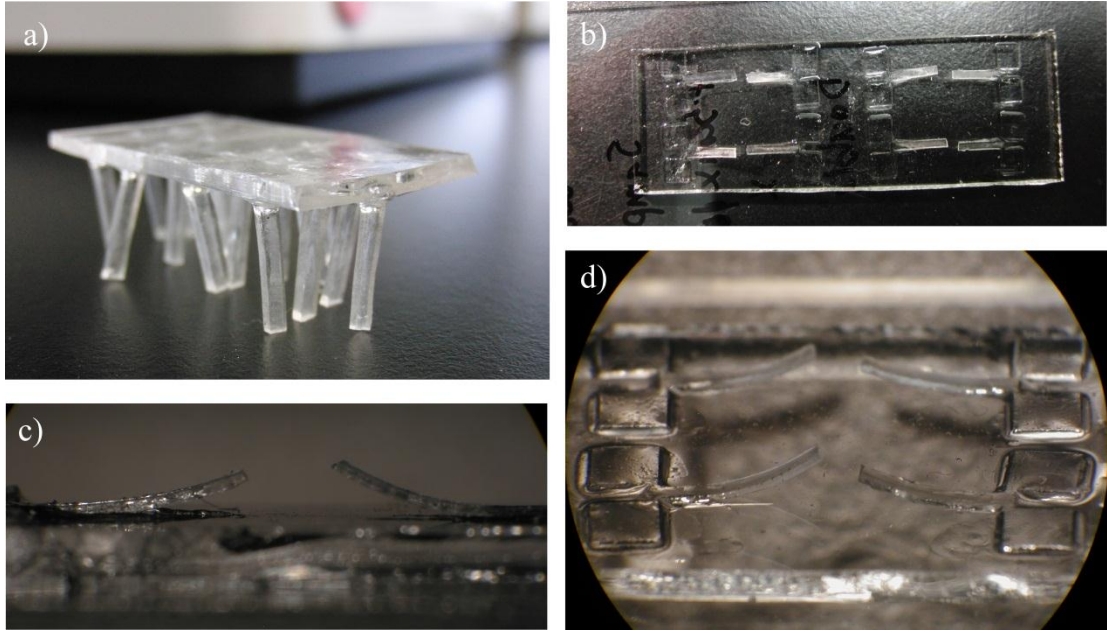
Figure 5.4: (a) All-PDMS robot mock-up, able to stand under its own weight. (b) Second mock-up (shown inverted) with 8 legs in the shape of 5 mm × 1 mm bending actuators. (c) Inverted side view of second mock-up showing leg profile. (d) Perspective view of second robot mock-up showing 4 of 8 legs.

As is evident from Figure 5.4c and d, the nature of the mechanical attachment caused the legs to rest at such an angle under the robot so that the second mock-up could not stand under its own weight. Therefore, care must be taken in determining how the legs should be mechanically attached to the robot body. This is all the more critical when one considers that the T-shaped configuration does not work for the DEAs (electrical shorting across electrodes) and has been replaced by the Y-shaped configuration that occupies more real estate on the robot body.

Not only does this configuration pose a challenge from a mechanical perspective, it also brings electrical repercussions: the matter of routing electrical signals to the DEA legs. If one decides to forgo the Y-configuration and its charge isolating properties, then for electrode lines (to the bottom and top of the robot body) or vias (conductive

pathways through the body itself), there are still complications caused by the need to insulate the lines from each other and the surroundings at such high voltages. Software developed for printed circuit board (PCB) design could be adapted to solve such routing problems while considering the unique challenges posed by the high voltage and mechanical attachment requirements of DEA legs.

5.5   Bending DEA Design

Should the DEA interactions and leg-to-robot body attachment issues be addressed, it is obvious that other challenges to the realization of DEA ambulated robots lay ahead: for example, issues stemming from the current bending DEA structure, fabrication, and operation. As discussed in Section 3.7, the bending DEAs were intended to act as both supports and actuators in their roles as robotic legs, and as such, possess a distributed compliance. One disadvantage of this design was that the legs occasionally had a rest position that was not straight but bent, due to the effects of residual stress. These effects are evident in pictures of the bending DEAs (Figures Figure 5.1 -Figure 5.4c and d) and undermine the ability of the DEA leg to support vertical loads as proposed in the robot walking gait (Section 3.3). The introduction of residual stress possibly occurred due to electrode deposition: while the Au electrode was sputtered, the PDMS substrate was heated, and expanded in accordance. Due to the mismatch in coefficients of thermal expansion of Au (14×10^{-6}/ °C [43]) and PDMS (310×10^{-6}/ °C [44]), compressive residual stress could have been introduced after cooling. Upon release, the stress caused the DEA to assume a bent shape. The mechanical action of the razor during the release process may have also played a role

73

in causing this bending. Solutions to residual stress effects may lie in alternative designs for the DEA legs and potentially, a reworking of the proposed gait.

Distributed compliance (the high flexibility of the entire leg structure) might also affect the DEA leg during operation. If the DEA leg is perturbed so that it is unable to execute the intended bending actuation, the robot may experience a catastrophic failure: it may simply be unable to ambulate, or the perturbation may be such that some DEA legs are unable to support their share of the payload properly, so that under the increased load other legs buckle and the robot collapses completely. A potential solution is the introduction of hyper-redundancy to the design in the form of duplicate sets of DEA legs that allow the robot to overcome some environmental hindrances. However, this solution introduces its own set of problems such as increased power requirements, decreased real estate on robot body, and larger robot size.

5.6 Conclusions

Serious challenges face the attachment of fabricated bending DEA legs to millimeter-scale robot bodies. Interactions between the DEA and their surroundings (including each other) serve to hinder their expected actuation behavior. The key to mitigating these interactions lies in the reduction of the actuation voltage (and electric field) but with the current materials and design, such actions result in diminished actuator performance. The nature of the mechanical attachments of the DEA legs to the robot body, as well as the electrical implications of those design decisions must be carefully considered. The current design of the DEA legs have inherent flaws that manifest in

both fabrication and operation, and could potentially hinder the robot's ambulation.

Thus, aspects of the bending DEA's design, fabrication and operation may need to be

re-envisioned.

Chapter 6: Conclusions & Future Work

6.1 Summary of Work & Results

In the work detailed in this thesis, we sought to develop millimeter-scale actuation technologies that would serve the purpose of ambulating robots in a robust and predictable manner. For this purpose, we selected a class of polymer actuators called dielectric elastomer actuators (DEAs) that promised simpler structures, larger strains and higher efficiencies over other technologies at the required size scale.

We began our study of DEAs by characterizing the simplest configuration capable of doing work: the uniaxial free-film configuration. We noted that the Maxwell stress equation over-predicts the actuation strain demonstrated by DEAs with this configuration and that the load curves possess a unique shape different from traditional linear actuators. During testing, it was observed that PDMS, although with the lowest actuation strain (smallest ε_r and highest modulus), showed significantly less creep than the other two materials, TC-5005 and VHB-4905, and ε_r frequency-independence. In other words, of the three elastomer materials, PDMS was the "best-behaved" in terms of predictability and controllability; the larger stiffness could be considered an advantage when payload capacity is considered. The experimental setup and testing procedure presented could serve as a new protocol for future material testing to identify an even better DEA elastomer than PDMS.

Two principles were then identified as means of converting in-plane strain to bending actuation for the purposes of ambulating a robot following the proposed walking gait.

Bending DEA samples were fabricated, tested, and it was concluded that the DEA utilizing the principle of an asymmetrical surface profile (crenellated) out-performed its counterpart which employed the principle of electrode stiffness differentials. The maximum displacement observed was 1.5 mm from a 10 mm long actuator.

In order to gauge the expected results from a DEA-ambulated robot, the optimization of bending DEA speed and payload was performed. For simplicity, electrode stiffness differential DEAs were used. They were modeled as slender load-bearing columns whose end displacement was dictated by Timoshenko bilayer bending. MATLAB code was written to perform the multi-objective optimization, and the results (6.88 m/s, 110 mg per leg) matched well to those measured for Ebefor's thermally-actuated walking robot. However, with the number of assumptions made, what seems to be significant sensitivity to changes in the fixed parameters, and potential modifications to the form and structure of the DEA leg, other models and/or optimization formulations may need to be developed.

This work concludes by noting the challenges associated with attaching DEAs to a robot body. Of special interest are the disruptive interactions of the DEAs with their surroundings, issues with attaching the DEAs both mechanically and electrically to the robot body, and potential ambulation-hindering issues inherent to the current DEA design. These problems will have to be solved by clever design decisions and better materials in the future.

6.2 Future Work

DEAs show potential for use in soft robotics applications. However, as discussed in Chapter 5, serious challenges remain that must be overcome before further progress can be made towards realizing their potential as actuators. In the short term, the next step should be experimentation to measure the force outputs of the bending actuators presented in Chapter 3. It is important that these values be determined so that the feasibility of use of these actuators may be established.

In the longer term, dedicated materials science research is needed to develop DEA elastomer materials that exhibit high strains like VHB-4905, low modulus like TC-5005, and possess low creep, ε_r frequency-independence, and design flexibility like PDMS. DEA modeling must also be re-examined: particularly, the effect of boundary conditions on expected device performance. In the literature, a lot of work has been committed to modeling and maximizing strain for DEA configurations that are too complex for the small scale, as well as characterizing materials like VHB-4905 that are not ideal for controlled applications such as robotics. The DEA's true promise is at smaller scales, where clever design and innovative materials work can combine to yield significant results.

6.3 Contributions

This research took concrete steps to explore the use of DEAs as an actuation technology for small scale robotics. The scientific contributions of this work are listed below.

1. Examined in depth, the elastomer material properties pertinent to the actuation strain of DEAs made from those elastomers.

    a. Comprehensively measured the relative dielectric permittivity, tangent modulus, and creep strain of three common DEA elastomers (PDMS, VHB-4905 and TC-5005) under identical laboratory conditions.

    b. Discovered the frequency dependence of the relative dielectric permittivity of TC-5005, a property not shared by the other two materials.

    c. Demonstrated that the stress-strain curves of all three materials are non-linear, and thus the tangent modulus should be used instead of the elastic modulus.

    d. Documented significant creep strain for VHB-4905 and TC-5005, which acts to hinder the controllability and high-frequency operation of their DEAs.

    e. Formulated, in the form of the presented experimental setup and procedure, a new protocol for future material testing to identify better DEA elastomers.

2. Characterized the planar DEA configuration.

    a. Identified a failure mechanism — shorting between electrodes across the side of a DEA film that is different from dielectric breakdown and that limits the maximum strain of planar DEAs.

    b. Compared the actuation strain of planar DEAs made from these three materials.

    c. Showed that for the planar configuration, the effects of boundary conditions, material properties and geometry are not accounted for by the Maxwell stress model.

    d. Produced a load curve for PDMS planar DEAs that define the work capabilities of these actuators.

3. Developed fabrication protocols for bending DEAs based on asymmetric surface profiles and electrode stiffness differentials.

4. Optimized electrode stiffness differential DEA design to maximize the speed and payload capabilities of a DEA-ambulated robot.

    a. Proposed a walking gait for a millimeter-scale robot using bending DEAs as legs.

    b. Formulated optimization problem by modeling DEA speed and payload capacity.

    c. Wrote MATLAB code to perform calculations.

5. Identified DEA interactions as a major challenge on the small scale.

Appendix A: Nomenclature

A	Cross sectional area (m^2)
b	Width (m)
C	Capacitance (F)
E	Elastic or tangent modulus (Pa)
e	Eccentricity (m)
f	Frequency (Hz)
h	Layer thickness (m)
I	Moment of Inertia (m^4)
L	Length (m)
P	Axial force/ load (N)
P_{cr}	Critical load for columnar buckling failure (N)
S	Strain (-)
t	Time (s)
U	Stored electrical energy for capacitor (J)
u	Speed (m/s)
V	Voltage (V)
v	Deflection of column in y-direction (m)

Greek Symbols

Δx	Actuator end displacement (m)
δ	Maximum deflection (y-direction) of column before buckling failure (m)
ε_0	Vacuum permittivity or permittivity of free space (F/m)
ε_r	Relative dielectric permittivity (-)
κ	Curvature (m^{-1})
ρ	Radius of curvature (m)
σ	Stress (Pa)
τ	Time constant (s)
υ	Poisson's ratio (-)

Appendix B: Supporting Information for Chapter 2

B.1 DEA Samples under Load

During the testing performed in this paper that involved the uniaxial loading of DEA samples, the occurrence of "necking' was observed, where the width of the sample shrunk in response to the elongation in the axial loading direction. This is illustrated in Figure 6.1.
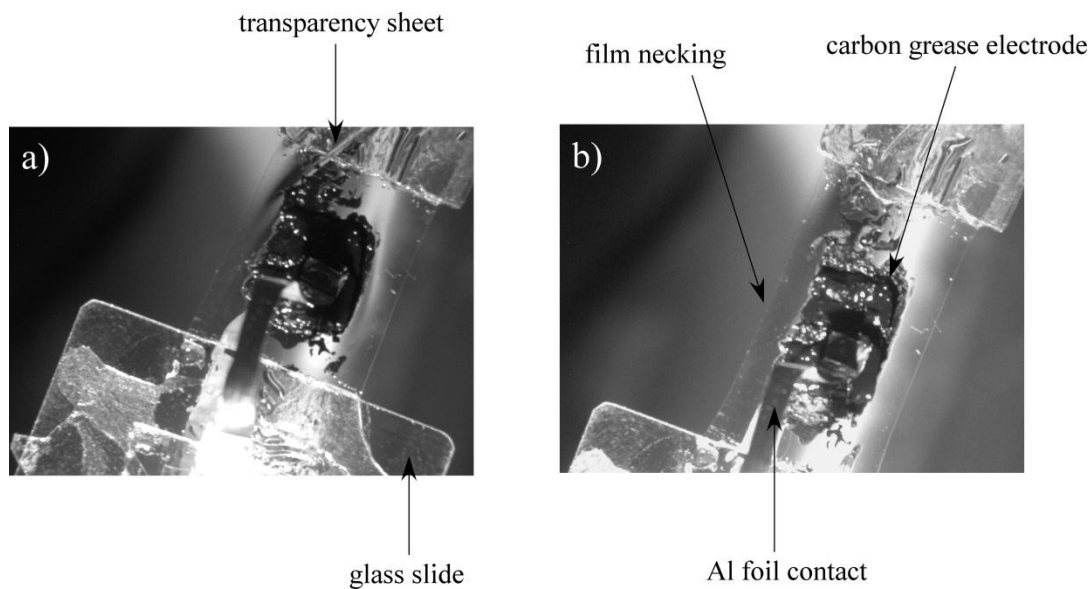
Figure 6.1: (a) DEA sample at zero load. (b) DEA sample exhibiting necking while the supporting a 49.5 g (1.1 MPa) load.

B.2 Stretch Ratio

PDMS films were strained beyond 30% and the layer thicknesses under various loads were measured using calipers. Normalized thickness (stretch ratio) for PDMS is shown as a function of stress for three samples in Figure 6.2. The films had starting thicknesses of 40 μm, measured using calipers with a resolution of 2 μm.
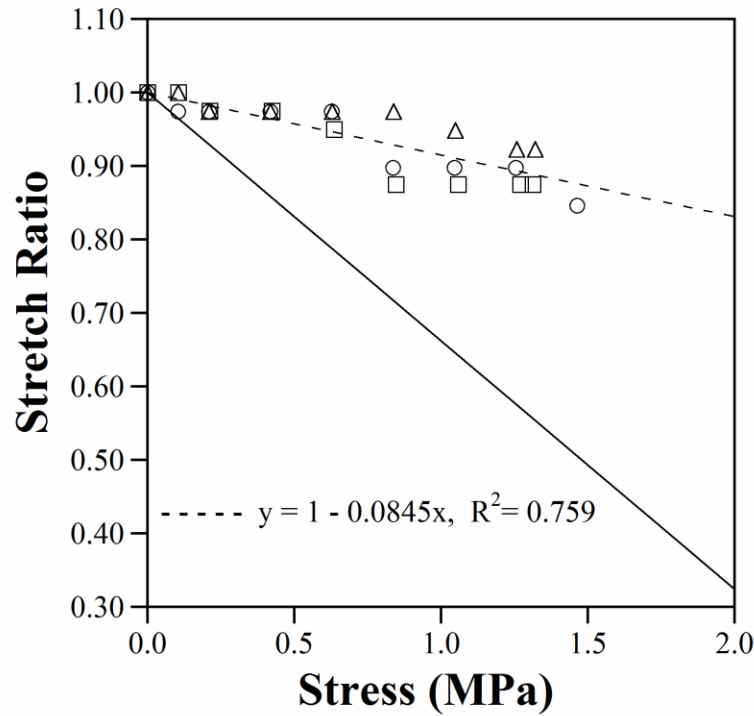
Figure 6.2: Stretch ratio (normalized thickness) of PDMS as a function of applied stress. The dashed line is the linear fit used to estimate the DEA thickness for the load-strain measurements in Figure 2.6. The expected stretch ratio, given by Equation 1.4 and based on the Poisson's ratio, is shown by the solid line.

Poisson's ratio predicts a relationship between transverse and lateral strain of

$$\lambda = \frac{L}{h} = -\left(\frac{v}{E}\right)\sigma + 1 \qquad (8.1)$$

where λ is the stretch ratio in the thickness direction, L is final sample length, h is the initial sample thickness, E is the tangent modulus (for PDMS, 1.06 MPa at 5% strain), and σ is the applied stress. The linear fit to the experimental data (dashed line) did not match the Poisson's ratio prediction (solid line). During testing, it was observed that the samples underwent necking, as shown in Figure 6.1. This phenomenon, in addition to the fact that the sample configuration (Figure 2.1) is not

purely uniaxial [10], is most likely the reason for this discrepancy. The linear fit to

the data was used to estimate the sample thickness of PDMS-based DEAs under load.

The thickness estimates were also used to determine the cross-sectional area needed

to calculate the stress from the load.

Appendix C: Optimization MATLAB Code

```matlab
% Bi-objective Optimization (Canned)
function multiUP
clear
clc

%define parameters
eps0=8.85e-12;
epsr=2.8;
nu=0.49;
i=0;
bwidth=1e-3; %Assume b=1mm
E1=80e9;

A=[];
b=[];
Aeq=[];
beq=[];
lb=[1e-8,1e-5,1e-3,0.8e6,0.1,0,0.1];
ub=[1e-6,1e-3,1e-2,1.8e6,100,6400,0.5];
x0=[5e-7,8e-4,1e-2,1.8e6,100,6400,0.5];
x0=(lb+ub)/2;
options=[];

%main optimization function
[x,fval]=fminimax(@MultiFunction,x0,A,b,Aeq,beq,lb,ub,@nonlinconM,op
tions,eps0,epsr,nu,E1,bwidth);
disp(['h1= ' num2str(x(1)),' h2= ' num2str(x(2)), ' L= '
num2str(x(3)), ' E2= ' num2str(x(4)), ' f= ' num2str(x(5)), ' V= '
num2str(x(6)),' niratio= ' num2str(x(7))])

disp([' Speed= ' num2str(-fval(1)*1000),' Payload= ' num2str(-
fval(2)*1000)])
% Speed in mm/sec, Payload in grams

end
end

%nonlinear constraint
function [C,Ceq]=nonlinconM(x,eps0,epsr,nu,E1,bwidth)
h1=x(1);
h2=x(2);
L=x(3);
E2=x(4);
f=x(5);
V=x(6);
niratio=x(7);

m=h1/h2;
n=E1/E2;

k=nu*eps0*epsr*((V/h2)^2)/(2*E2*h2)*(6*m*n*(1+m))/(1+(4*m*n)+(6*m^2*
n)+(4*m^3*n)+(m^4*n^2));
```

```matlab
rho=1/k;

C(1)=L/rho-0.1;
C(2)=0.01-L/rho;
Ceq=[];
end

%objective function
function Multi=MultiFunction(x,eps0,epsr,nu,E1,bwidth)
h1=x(1);
h2=x(2);
L=x(3);
E2=x(4);
f=x(5);
V=x(6);
niratio=x(7);

m=h1/h2;
n=E1/E2;

k=nu*eps0*epsr*((V/h2)^2)/(2*E2*h2)*(6*m*n*(1+m))/(1+(4*m*n)+(6*m^2*
n)+(4*m^3*n)+(m^4*n^2));
rho=1/k;
deltax=rho*(1-cos(L/rho));
U=-deltax*f;

Enet=E2; % Assumed that Enet = E2=E(PDMS)
Pcr=0.1705*(pi()^2)*Enet*bwidth*((h1+h2)^3)/(L^2);
P=-(Pcr*((2/pi()*asec(niratio+1))^2));

Multi(1)=U;
Multi(2)=P;
End
```

Appendix D: DEA Laser Machining

DEA laser machining involves the use of lasers to "cut out" and release batch-fabricated DEAs. It was explored as a means of easing DEA sample fabrication, increasing throughput, and reducing measurement errors due to sample dimension variation. Recently, Maleki et al. [12] laser machined millimeter-scale bending DEAs with a PDMS base and carbon grease electrodes.

Laser machining was achieved using an automated laser platform (Universal Laser Systems VersaLaser VLS 3.60, Figure 6.3a), programmed to trace out the outline of a DEA sample. Testing began by exploring the settings required to properly machine pieces of 200 μm thick PDMS as surrogates for a 135 ± 26 μm DEAs. The best settings are shown in Table 6.1, and the results are shown in Figure 6.3b and c.

Table 6.1: Best settings of laser platform for PDMS machining

Material	Power	Speed	PPI (Pulse per inch)
Plastics (Acrylics)	30 %	50 %	1000
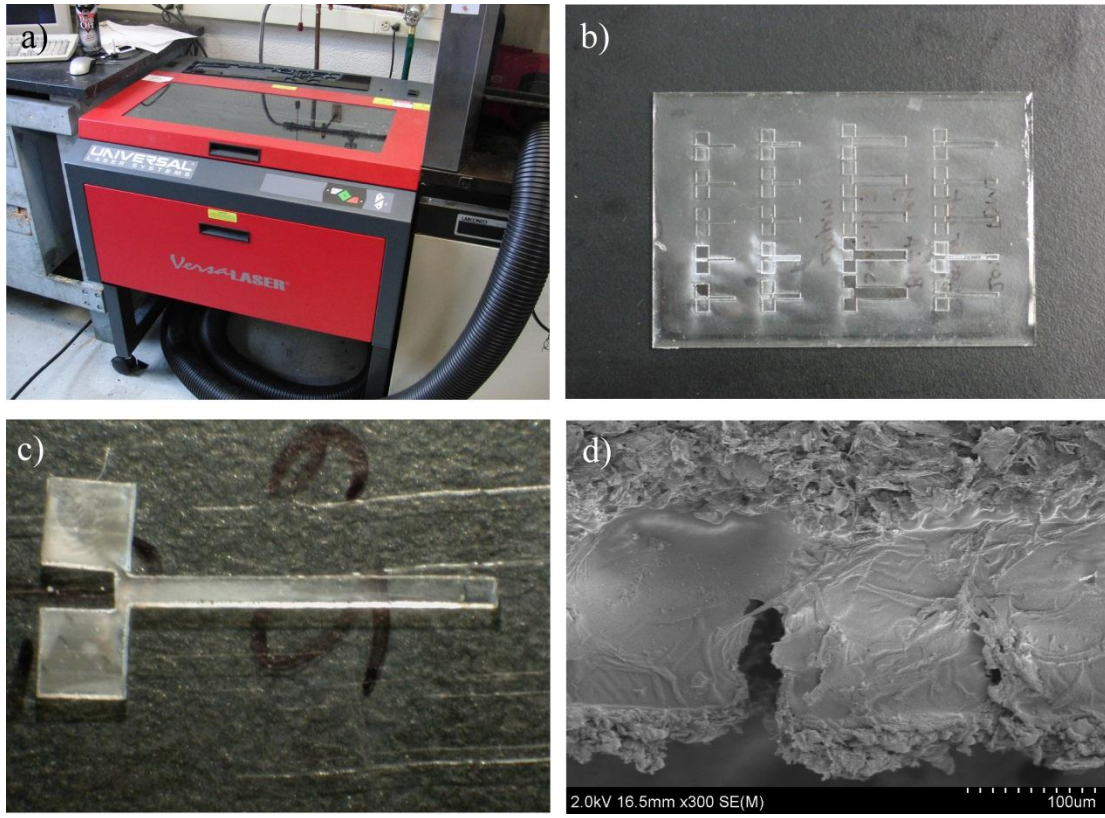
Figure 6.3: Laser platform (courtesy of Advanced Manufacturing Lab). (b) Laser machined 200 μm PDMS showing arrays of actuators (T-shaped). (c) Laser machined and released PDMS shape. (d) SEM image of laser machined cross-section of crenellated DEA with sprayed PDMS/EG electrodes on both sides.

After establishing a procedure for the laser machining, the process was integrated into the fabrication protocol for bending DEAs. During tests for the conformity of electrodes on crenellated PDMS surfaces (Section 3.5.2), DEA samples were fabricated and laser machined. As shown in Figure 6.3d, the laser successfully cut across the PDMS and PDMS/EG electrodes, although the otherwise smooth PDMS surface was scarred in the process. In subsequent tests, the laser was successfully used to machine Au-coated PDMS surfaces with the same settings.

However, because the electrode application steps in the fabrication protocol came before the automated laser machining step and involved the manual transfer of films from one carrier (glass slide) to another, misalignments occurred, resulting in the laser ablating outside the required outline. Thus throughput (the percentage of properly shaped actuators realized) fell (30%). This, coupled with the aforementioned faults with the T-shaped DEA (dielectric breakdown between electrode contact pads), resulted in a cessation of further exploration of laser machining as a fabrication step.

The laser machining process remains a viable addition to DEA fabrication protocol in the future. The work presented in this appendix should provide a sufficient foundation on which to build, should the need ever arise.

References

[1]   J. Kim, S. E. Chung, S.-E. Choi, H. Lee, J. Kim, and S. Kwon, "Programming magnetic anisotropy in polymeric microactuators," *Nat Mater,* vol. 10, pp. 747-752, 2011.

[2]   J. R. Bronson, J. S. Pulskamp, R. G. Polcawich, C. M. Kroninger, and E. D. Wetzel, "PZT MEMS Actuated flapping wings for insect-inspired robotics," in *IEEE Micro Electro Mechanical Systems* Sorrento, Italy: IEEE, 2009.

[3]   R. J. Wood, "The first takeoff of a biologically inspired at-scale robotic insect," *Ieee Transactions on Robotics,* vol. 24, pp. 341-347, Apr 2008.

[4]   E. Y. Erdem, Y. M. Chen, M. Mohebbi, J. W. Suh, G. T. A. Kovacs, R. B. Darling, and K. F. Bohringer, "Thermally Actuated Omnidirectional Walking Microrobot," *Journal of Microelectromechanical Systems,* vol. 19, pp. 433-442, Jun 2010.

[5]   T. Ebefors, J. U. Mattsson, E. Kalvesten, and G. Stemme, "A Walking Silicon Micro-Robot," in *Solid-State Sensors and Actuators (Transducers'99)* Sendai, Japan, 1999.

[6]   Q. Pei, R. Pelrine, M. Rosenthal, S. Stanford, H. Prahlad, and R. Kornbluh, "Recent progress on electroelastomer artificial muscles and their application for biomimetic robots," in *Smart Structures and Materials 2004: Electroactive Polymer Actuators and Devices (EAPAD)*, San Diego, CA, 2004, pp. 41 - 50.

[7]   R. Pelrine, R. Kornbluh, J. Joseph, R. Heydt, Q. Pei, and S. Chiba, "High-field deformation of elastomeric dielectrics for actuators," *Materials Science and Engineering C - Biomimetic Supramolecular Systems,* vol. 11, pp. 89-100, Sep 2000.

[8]   R. Pelrine, R. Kornbluh, and J. Joseph, "Electrostriction of polymer dielectrics with compliant electrodes as a means of actuation," *Sensors and Actuators A-Physical,* vol. 64, pp. 77-85, 1 January 1998 1998.

[9]   R. Pelrine, R. Kornbluh, Q. Pei, S. Stanford, S. Oh, J. Eckerle, R. J. Full, M. Rosenthal, and K. Meijer, "Dielectric Elastomer Artificial Muscle Actuators: Toward Biomimetic Motion," in *Smart Structures and Materials 2002: Electroactive Polymer Actuators and Devices (EAPAD)*, San Diego, CA, 2002, pp. 126 - 137.

[10]   G. Yang, W. Ren, and B. K. Mukherjee, "Characterization of the transverse elongation of polymeric electrostatic actuators induced by Maxwell stress," *IEEE TDEI,* vol. 1, pp. 81-88, 2011.

[11]   O. A. Araromi, A. T. Conn, C. S. Ling, J. M. Rossiter, R. Vaidyanathan, and S. C. Burgess, "Spray deposited multilayered dielectric elastomer actuators," *Sensors and Actuators a-Physical,* vol. 167, pp. 459-467, Jun 2011.

[12]   T. Maleki, G. Chitnis, and B. Ziaie, "A batch-fabricated laser-micromachined PDMS actuator with stamped carbon grease electrodes," *Journal of Micromechanics and Microengineering,* vol. 21, Feb 2011.

[13]   C. Jordi, A. Schmidt, G. Kovacs, S. Michel, and P. Ermanni, "Performance evaluation of cutting-edge dielectric elastomers for large-scale actuator applications," *Smart Materials & Structures,* vol. 20, Jul 2011.

[14]   F. Carpi, G. Gallone, F. Galantini, and D. De Rossi, "Silicone-poly(hexylthiophene) blends as elastomers with enhanced electromechanical transduction properties," *Advanced Functional Materials,* vol. 18, pp. 235-241, Jan 24 2008.

[15]   H. Kim, S. Hwang, H. R. Choi, H. M. Kim, J. W. Jeon, and J.-D. Nam, "Field actuated behavior of polymers as dielectric material," in *Smart Structures and Materials 2001: Electroactive Polymer Actuators and Devices (EAPAD)*, San Diego, CA, 2001, pp. 491-498.

[16]   G. Kofod, P. Sommer-Larsen, R. Kronbluh, and R. Pelrine, "Actuation response of polyacrylate dielectric elastomers," *Journal of Intelligent Material Systems and Structures,* vol. 14, pp. 787-793, Dec 2003.

[17]   C. Jean-Mistral, A. Sylvestre, S. Basrour, and J. J. Chaillout, "Dielectric properties of polyacrylate thick films used in sensors and actuators," *Smart Materials & Structures,* vol. 19, pp. -, Jul 2010.

[18]   G. Kofod and P. Somrner-Larsen, "Some aspects of large strain actuation in dielectric elastomers," in *12th International Symposium on Electrets, 2005 (ISE-12)*, Bahia, Brazil, 2005, pp. 208-211.

[19]   T. G. McKay, E. P. Calius, and I. A. Anderson, "The dielectric constant of 3M VHB: a parameter in dispute," in *Smart Structures and Materials & Nondestructive Evaluation and Health Monitoring 2009: Electroactive Polymer Actuators and Devices (EAPAD)*, San Diego, CA, USA 2009, p. 72870P.

[20]   W. Ma and L. E. Cross, "An experimental investigation of electromechanical response in a dielectric acrylic elastomer," *Applied Physics A-Materials Science & Processing,* vol. 78, pp. 1201-1204, May 2004.

[21]   M. Wissler and E. Mazza, "Electromechanical coupling in dielectric elastomer actuators," *Sensors and Actuators a-Physical,* vol. 138, pp. 384-393, Aug 26 2007.

[22]   H. Fröhlich, *Theory of dielectrics*, 2nd ed. London: Oxford University Press 1958.

[23]   J. P. Rolland, R. M. Van Dam, D. A. Schorzman, S. R. Quake, and J. M. DeSimone, "Solvent resistant photocurable "liquid teflon" for microfluidic device fabrication (vol 126, pg 2322, 2004)," *Journal of the American Chemical Society,* vol. 126, pp. 8349-8349, Jul 7 2004.

[24]   F. Schneider, T. Fellner, J. Wilde, and U. Wallrabe, "Mechanical properties of silicones for MEMS," *Journal of Micromechanics and Microengineering,* vol. 18, pp. -, Jun 2008.

[25]   G. Gallone, F. Carpi, D. De Rossi, G. Levita, and A. Marchetti, "Dielectric constant enhancement in a silicone elastomer filled with lead magnesium niobate-lead titanate," *Materials Science & Engineering C-Biomimetic and Supramolecular Systems,* vol. 27, pp. 110-116, Jan 2007.

[26]   S. Ha, W. Yuan, Q. Pei, R. Pelrine, and S. Stanford, "Interpenetrating polymer networks for high-performance electroelastomer artificial muscles," *Advanced Materials,* vol. 18, pp. 887-891, Apr 2006.

[27]   W. N. Findley, J. S. Lai, and K. Onaran, *Creep and relaxation of nonlinear viscoelastic materials* vol. 371. New York: Dover Publications Inc, 1989.

[28]   Y. Jhong, D. Mikolas, T. Yeh, W. Fang, D. Shaw, J. Chen, and C. Fu, "Characterization of nonlinear effects in a two-dimensional dielectric elastomer actuator," *Smart Materials & Structures,* vol. 19, Oct 2010.

[29]   G. Jordan, D. N. McCarthy, N. Schlepple, J. Krissler, H. Schroder, and G. Kofod, "Actuated Micro-optical Submount Using a Dielectric Elastomer Actuator," *Ieee-Asme Transactions on Mechatronics,* vol. 16, pp. 98-102, Feb 2011.

[30]   M. Ashby, H. Shercliff, and D. Cebon, *Materials: Engineering, science, processing and design*, 1st ed. Italy: Butterworth-Heineman, 2007.

[31]   C. G. Cameron, J. P. Szabo, S. Johnstone, J. Massey, and J. Leidner, "Linear actuation in coextruded dielectric elastomer tubes," *Sensors and Actuators a-Physical,* vol. 147, pp. 286-291, Sep 15 2008.

[32]   R. Trujillo, J. Mou, P. E. Phelan, and D. S. Chau, "Investigation of electrostrictive polymers as actuators for mesoscale devices," *International Journal of Advanced Manufacturing Technology,* vol. 23, pp. 176-182, Feb 2004.

[33]   F. Carpi and D. De Rossi, "Dielectric elastomer cylindrical actuators: electromechanical modelling and experimental evaluation," *Materials Science & Engineering C-Biomimetic and Supramolecular Systems,* vol. 24, pp. 555-562, Jun 2004.

[34]   A. Pimpin, Y. Suzuki, and N. Kasagi, "Microelectrostrictive actuator with large out-of-plane deformation for flow-control application," *Journal of Microelectromechanical Systems,* vol. 16, pp. 753-764, Jun 2007.

[35]   I. Diaconu, A. David, and D. O. Dorohoi, "An experimental investigation of electroactive polyurethane," *Journal of Optoelectronics and Advanced Materials,* vol. 7, pp. 2797-2801, Dec 2005.

[36]   M. R. Kessler and R. Palakodeti, "Influence of frequency and prestrain on the mechanical efficiency of dielectric electroactive polymer actuators," *Materials Letters,* vol. 60, pp. 3437-3440, Dec 2006.

[37]   T. Maleki, G. Chitnis, A. Panja, and B. Ziaie, "Single-layer elastomeric out-of-plane actuator with asymmetric surface profile," in *Solid-State Sensors, Actuators, and Microsystems Workshop* Hilton Head Island, SC, 2010.

[38]   G. K. Lau, S. C. K. Goh, and L. L. Shiau, "Dielectric elastomer unimorph using flexible electrodes of electrolessly deposited (ELD) silver," *Sensors and Actuators a-Physical,* vol. 169, pp. 234-241, Sep 10 2011.

[39]   M. Kujawski, J. D. Pearse, and E. Smela, "Elastomers filled with exfoliated graphite as compliant electrodes," *Carbon,* vol. 48, pp. 2409-2417, Aug 2010.

[40]   R. S. Dhariwal, J. M. Torres, and M. P. Y. Desmulliez, "Electric field breakdown at micrometre separations in air and nitrogen at atmospheric pressure," *Ieee Proceedings-Science Measurement and Technology,* vol. 147, pp. 261-265, Sep 2000.

[41]   S. Timoshenko, "Analysis of bi-metal thermostats," *Journal of the Optical Society of America,* vol. 11, pp. 233–256, 1925.

[42]   J. M. Gere, *Mechanics of materials*, 6th ed. Canada: Brooks/Cole - Thomson Learning, 2004.

[43]   F. C. Nix and D. MacNair, "The Thermal Expansion of Pure Metals: Copper, Gold, Aluminum, Nickel, and Iron," *Physical Review,* vol. 60, pp. 597-605, 1941.

[44]   H. S. Chuang and S. Wereley, "Design, fabrication and characterization of a conducting PDMS for microheaters and temperature sensors," *Journal of Micromechanics and Microengineering,* vol. 19, Apr 2009.